Supporting Information

Rapid formation of aerosol precursors from the autoxidation of aromatic carbonyls and the remarkable enhancing influence of NO addition

Shawon Barua[1,*], Avinash Kumar[1], Prasenjit Seal[1], Mojtaba Bezaatpour[1], Sakshi Jha[1], Nanna Myllys[2], Siddharth Iyer[1], and Matti Rissanen[1,2,*]

[1]Aerosol Physics Laboratory, Physics Unit, Faculty of Engineering and Natural Sciences, Tampere University, 33720 Tampere, Finland

[2]Department of Chemistry, University of Helsinki, P.O. Box 55, FI-00014 Helsinki, Finland

*Correspondence to: shawon.barua@tuni.fi, matti.rissanen@tuni.fi

S1. Tampere flow reactor setup

A schematic of the borosilicate glass flow reactor setup is shown in Figure S1. All the reactant gas supply lines are connected to the reactor via PTFE tubing and Swagelok fittings. The gas flows are controlled by Alicat mass flow controllers (MFC). The mass spectrometer inlet flow (8.1 lpm) and the volume of the reactor (1 m length and 4.7 cm inside diameter) defines the residence time of the reaction mixture inside the reactor. Short residence time experiments are achieved by providing the precursor VOC flow via a movable injector tube within the reactor and adjusting the distance of the injector tip with respect to the mass spectrometer orifice. The deuterated water (D_2O) line and the NO line were used separately only during the hydrogen to deuterium (H/D) exchange experiment and the oxidation experiment in presence of NO, respectively.

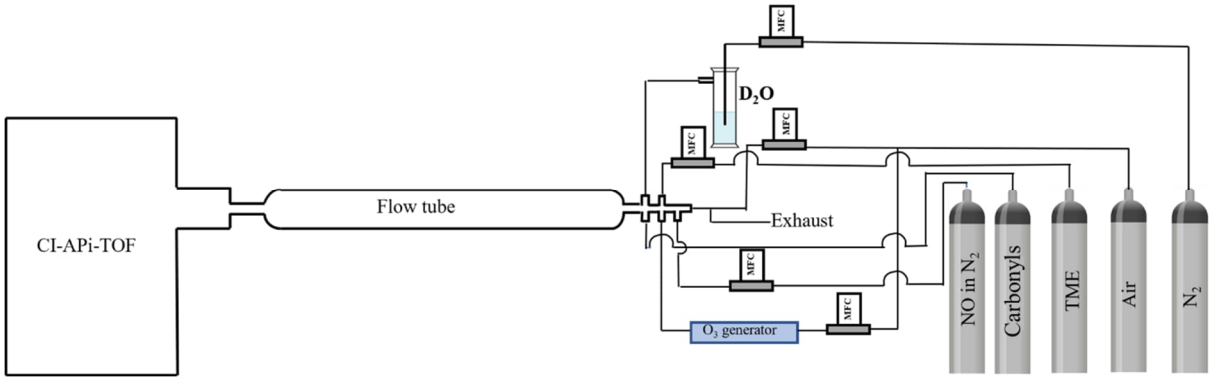

Figure S1. A nitrate (NO_3^-) based chemical ionization mass spectrometer coupled to ambient pressure flow reactor. TME = tetramethylethylene.

S2. Conformational sampling analysis

The conformers are generated by varying all torsional angles of each molecular species by 120º. Single-point quantum chemical calculations are performed on the conformers generated using the Spartan '20 program at B3LYP/6-31+G* level of theory using Gaussian 16 code. Only those within 5 kcal/mol in relative electronic energies with respect to the minimum energy geometry are considered for subsequent geometry optimizations. For the H-shift transition states (TS), we first constrain the H atom at an approximate distance from the relevant C and O atoms and then optimize the structure at B3LYP/6-31+G* level of theory. The optimized geometry is then used as an input for an unconstrained TS calculation. Once the TS geometry is found, an MMFF conformer sampling was carried out using Spartan′20 with the O---H and H---C bond lengths constrained. The partial bonds with torsions enabled are added to these two crucial bonds prior to the conformer sampling. The partial bonds results in improving the MMFF optimization, which in turn, provides geometries that are closer to local energy minima during the conformer sampling. After the initial sorting of the conformers, two sets of optimizations are performed, the first of which is done at B3LYP/6-31+G* (low-DFT) level of theory and structures within 2.0 kcal/mol of the minimum are then further re-optimized at ωB97X-D/aug-cc-pVTZ (high-DFT) to get the global minimum geometry. Finally, we perform energy refinement of the global minimum structure at ROHF-ROCCSD(T)-F12a/VDZ-F12 level of theory employing MOLPRO 2022.2. This energy refinement is done to get accurate and reliable energies for the estimation of the rate coefficients for some of the crucial autoxidation steps.

S3. OH addition versus H-abstraction predicted by SAR

The aromatic carbonyl OH oxidation can be initiated either by an H atom abstraction by OH from the substituent group of the phenyl ring or by the addition of the OH radical to the ring. To estimate the branching ratios between the two, we calculate the rate coefficients of the initial step of aromatic carbonyl OH oxidation reaction based on structure-activity relationship (SAR) data available in the literature.[1,2] The H-abstraction rate coefficients are calculated by using the formula, $k_{abs} = k_a \times F(X) \times F(Y)$ reported by Jenkin et al.[1] and Ziemann et al.[2] Here, k_a indicates the rate coefficient associated with the group (–C(O)H), –CH_2–, –CH_3) from which the H atom is being abstracted, where F(X) and F(Y) are the substituent group factors. In phenylacetaldehyde, for aldehydic H-abstraction, the substituent group factor F(X) corresponds to a –CH_2– group. For a secondary H-abstraction from the –CH_2–, the substituent group factors F(X) and F(Y) correspond to –C(O)H and –Ph groups respectively.

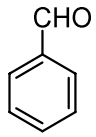

Benzaldehyde

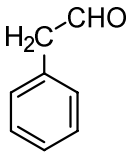

Phenylacetaldehyde

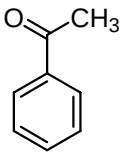

Acetophenone

The OH addition rate coefficients are calculated by using the formula, $\log k_{add} = -11.71 - 1.34 \times \Sigma\sigma^{+}$. In this approach, rate constants are calculated from a correlation between the rate constants and the sum of the electrophilic substituent constants $\Sigma\sigma^{+}$.[2] In all aromatic carbonyls, the values of substitution constant relative to *meta* position σ^{+}_{meta} are also used for *ipso* position as suggested by Ziemann et al.[2] for substituted aromatics. In benzaldehyde, we do not find a $\sigma^{+}_{ortho,para}$ for –CHO and we take the substituent constant from that of a closest match –C(O)OH for OH addition to *ortho* and *para* positions. In phenylacetaldehyde, we do not find either of $\sigma^{+}_{ortho,para}$ and σ^{+}_{meta} for $–CH_2CHO$ and we take the substituent constants from a closest functional group $–CH_2C(O)OCH_2CH_3$. Similarly, in acetophenone, due to the unavailability of $\sigma^{+}_{ortho,para}$ and σ^{+}_{meta} for $–C(O)CH_3$, we take the substituent constants from –C(O)OH group.[2] All the rate coefficients calculated using SAR are shown in Tables S1–3.

Table S1. Rate coefficients (in cm^3 $molecule^{-1}$ s^{-1}) of H-abstraction and OH addition reactions in benzaldehyde OH oxidation predicted by SAR.

H-abstraction; BR_{abs} = 85.52 %				
Abstraction site	$k_a^{\dagger}$	**F(X)**‡	k_{abs}	**BR (%)**
–CHO	20.8×10^{-12}	1 (X = –Ph)	2.08×10^{-11}	85.52
OH addition; BR_{add} = 14.48 %				
Addition site	**σ**	**σ^{+}**	k_{add}	**BR (%)**
Ipso	1	0.36	6.42×10^{-13}	2.64
Ortho	2	0.421	$2 \times (5.32 \times 10^{-13})$	4.37
Meta	2	0.36	$2 \times (6.42 \times 10^{-13})$	5.28
Para	1	0.421	5.32×10^{-13}	2.19

σ = symmetry factor. BR = branching ratio. $k_{overall} = 2.43 \times 10^{-11}$ cm^3 $molecule^{-1}$ s^{-1}.

† Values taken from Jenkin et al.[1] ‡ Values taken from Ziemann et al.[2]

Table S2. Rate coefficients of H-abstraction and OH addition reactions in phenylacetaldehyde OH oxidation predicted by SAR.

H-abstraction; BR_{abs} = 62.48 %				
Abstraction site	$k_a^{\dagger}$	**F(X)‡, F(Y)‡**	k_{abs}	**BR (%)**
–CHO	20.8×10^{-12}	1.23 (X = $–CH_2–$)	2.56×10^{-11}	61.10
$–CH_2–$	0.77×10^{-12}	0.75 (X = –CHO)	5.78×10^{-13}	1.38
		1 (Y = –Ph)		
OH addition; BR_{add} = 37.52 %				
Addition site	**σ**	**σ^+**	k_{add}	**BR (%)**
Ipso	1	-0.01	2.01×10^{-12}	4.80
Ortho	2	-0.164	$2 \times (3.23 \times 10^{-12})$	15.42
Meta	2	-0.01	$2 \times (2.01 \times 10^{-12})$	9.59
Para	1	-0.164	3.23×10^{-12}	7.71

σ = symmetry factor. BR = branching ratio. $k_{overall} = 4.19 \times 10^{-11}$ cm^3 $molecule^{-1}$ s^{-1}.
† Values taken from Jenkin et al.[1] ‡ Values taken from Ziemann et al.[2]

Table S3. Rate coefficients of H-abstraction and OH addition reactions in acetophenone OH oxidation predicted by SAR.

H-abstraction; BR_{abs} = 2.53 %				
Abstraction site	$k_a^{\dagger}$	**F(X)‡**	k_{abs}	**BR (%)**
$–CH_3$	0.13×10^{-12}	0.75 (X = –C(O)–)	9.75×10^{-14}	2.53
OH addition; BR_{add} = 97.47 %				
Addition site	**σ**	**σ^+**	k_{add}	**BR (%)**
Ipso	1	0.322	7.22×10^{-13}	18.71
Ortho	2	0.421	$2 \times (5.32 \times 10^{-13})$	27.57
Meta	2	0.322	$2 \times (7.22 \times 10^{-13})$	37.41
Para	1	0.421	5.32×10^{-13}	13.78

σ = symmetry factor. BR = branching ratio. $k_{overall} = 3.86 \times 10^{-12}$ cm^3 $molecule^{-1}$ s^{-1}.
† Values taken from Jenkin et al.[1] ‡ Values taken from Ziemann et al.[2]

S4. Formation of ipso bicyclic peroxy radical (i-BPR)

The first carbon centered radical ($C_xH_{y+1}O_2$ in Figure S2) formed via OH addition to the studied aromatic carbonyls can subsequently lead to non-fragmented oxidation products. The OH addition can take place at different positions of the phenyl ring, all of which can lead to the formation of bicyclic peroxy radicals (BPR). Recently, the formation of ipso-BPR intermediate (initial OH addition to the carbon with a substituent group) and its subsequent ring-fragmenting rearrangement reaction has been found to be crucial for rapid formation of highly oxygenated organic molecules (HOMs) in aromatics and has been well established for toluene autoxidation.[3] Therefore, we focus on this intermediate to find reaction routes to explain the observed HOMs in aromatic carbonyl OH oxidation experiments. The computed rates and branching ratios for the two possible ipso-BPR rearrangement reactions (see Figure 5 in the main manuscript) are given in Tables S4.

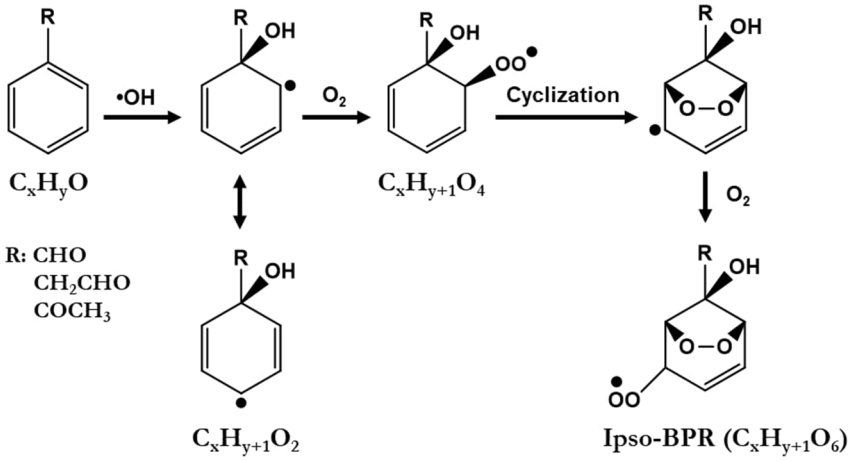

Figure S2. An example of the formation of a bicyclic peroxy radical (BPR, $C_xH_{y+1}O_6$) in OH initiated oxidation of aromatic carbonyls showing the initial addition of OH to the carbon with the substituent group (R: CHO/CH_2CHO/$COCH_3$), i.e., ipso position.

Table S4. Ipso-BPR opening energetics, rates, and branching ratios.

Ipso-BPR

ROHF-ROCCSD(T)-F12a/VDZ-F12//DFT-methods

Ipso-BPR (ΔE=0)	$\Delta E_{C1\ channel}$† (kcal/mol)		Rates (s^{-1})	Branching Ratio (%)	$\Delta E_{C2\ channel}$† (kcal/mol)		Rates (s^{-1})	Branching Ratio (%)
	TS	RB-C1‡			TS	RB-C2‡		
PhCHO	21.2	- 51.8	2.9 x **10^{-3}**	**36.7**	20.5	- 48.2	5.0 x **10^{-3}**	**63.3**
$PhCH_2CHO$	20.2	- 52.6	1.0 x **10^{-2}**	**1.6**	17.9	- 48.9	0.6	**98.4**
$PhCOCH_3$	22.3	- 54.6	5.4 x **10^{-4}**	**9.3**	20.6	- 48.2	5.3 x **10^{-3}**	**90.7**

† Ipso-BPR rearrangement channels. ‡ Ring broken peroxy radical intermediates.

S5. CO elimination versus O_2 addition

The aldehydic H-abstractions in PhCHO and $PhCH_2CHO$ readily form benzoyl (PhCO) and phenylacetyl ($PhCH_2CO$) radicals, respectively. The methyl H-abstraction in $PhCOCH_3$ form an alkyl radical ($PhCOCH_2$) followed by the formation of alkoxy radical $PhCOCH_2O$ in the latter steps (see Figure S3). One possible way to form the observed fragmented products (with $C_{x-1,2}$) can be associated with the H-abstraction channel. In $PhCH_2CHO$ and $PhCOCH_3$, our calculation shows that a CO elimination ($k = 3.1 \times 10^7 s^{-1}$) and an alkoxy β-scission ($k = 1.2 \times 10^9 s^{-1}$) reaction with HCHO loss, respectively, are likely feasible. In contrast, in PhCHO, the CO elimination ($k = 1.4 \times 10^{-4} s^{-1}$) from benzoyl radical intermediate is very slow. The subsequent reactions can allow the elimination of a CO_2 molecule ($k = 9.6 \times 10^8 s^{-1}$) from the benzoyloxy radical (PhC(O)O) intermediate (see Figure S3).

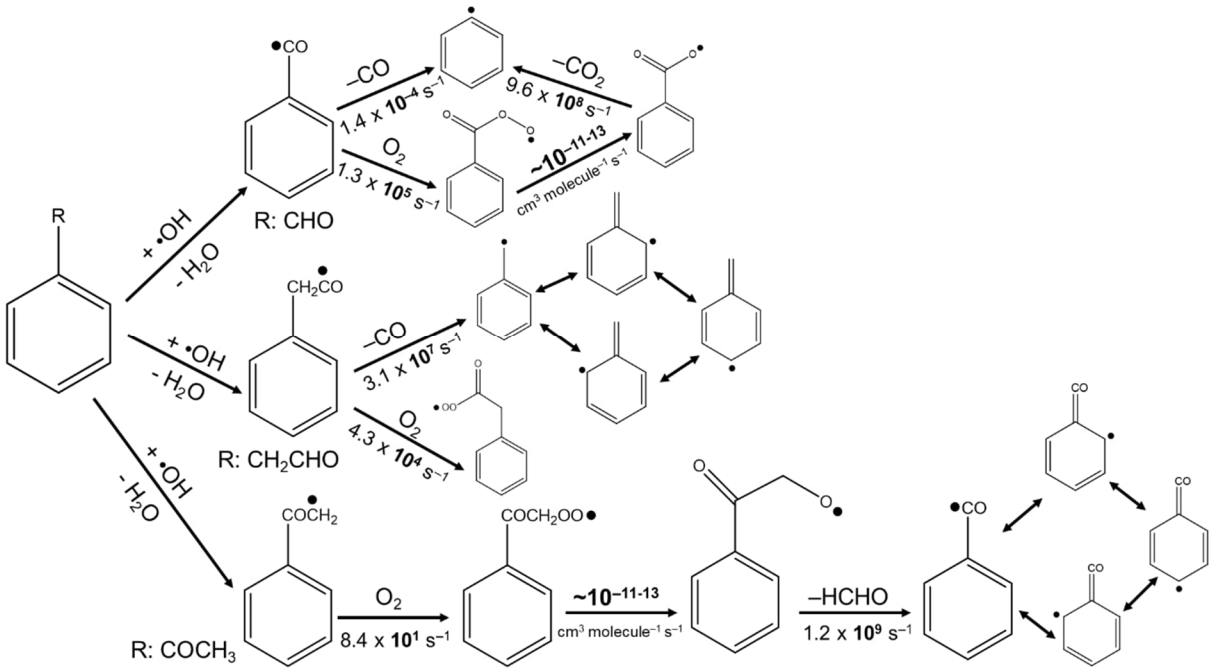

Figure S3. The kinetics of the CO elimination and O_2 additions in aromatic carbonyl OH oxidation. The peroxy-alkoxy rates (R'O_2 to R'O) were assumed to lie between 10^{-11} and 10^{-13} $cm^3 molecule^{-1} s^{-1}$. The rate coefficients were obtained using the M08-HX/def2-TZVP level of theory. No conformer sampling was performed.

S6. Formation of Nitrophenol from benzaldehyde oxidation in presence of NO_x

The fast aldehydic H-abstraction by oxidant OH in benzaldehyde forms a carbon centered benzoyl radical (PhCO). The PhCO rapidly adds an O_2 molecule and forms a benzoyl peroxy radical ($PhC(O)O_2$) intermediate (see Figure S4). The reaction of $PhC(O)O_2$ with itself or with other reaction partners, e.g., RO_2, HO_2, and most importantly NO in this case, can form benzoyloxy radical of PhC(O)O which loses a CO_2 molecule yielding a benzyl radical. The benzyl radical upon O_2 addition followed by another bimolecular reaction, e.g., with NO, form the benzoxy radical (PhO). Finally, a reaction between the PhO radical and NO_2 forms nitrophenol that involves an intramolecular H-shift from C2 (where the NO_2 is attached) to the O atom at C1.

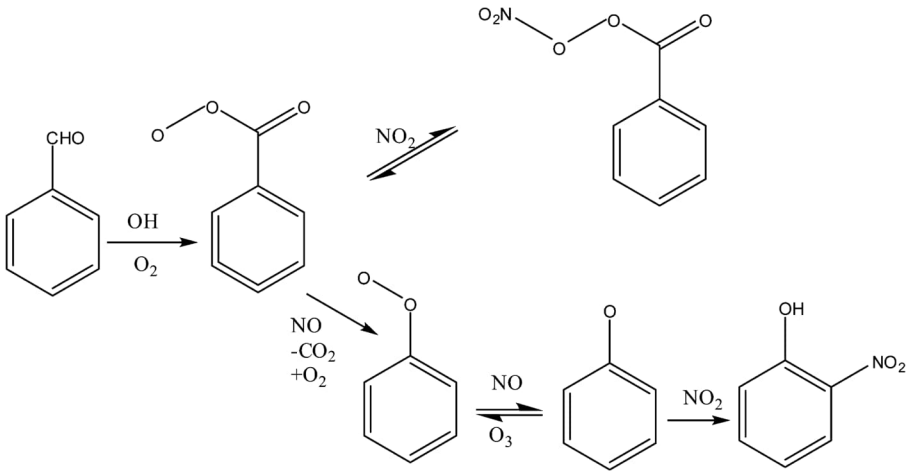

Figure S4. Atmospheric degradation of benzaldehyde involving oxidation initiated by OH radical to form nitrophenol (adapted from Calvert et al.).[4]

S7. Computational exploration via H-abstraction channel in benzaldehyde

We looked at the possible isomerization reactions of $PhC(O)O_2$ to find a gateway to HOM along the H-abstraction channel. The peroxy O atom of the $PhC(O)O_2$ may attach to any of the double bonds in the aromatic moiety (i.e., ortho, meta, and para positions) and form carbon centered radicals with an additional five-to-seven-member ring. It may also undergo H-shift reactions with the secondary carbons at those positions in the aromatic moiety. However, our calculated reaction rate barriers (in kcal/mol at ωB97X-D/6-31+G* level of theory) for these reactions are very high (see Table S5) and suggest that these isomerization reactions are unlikely to happen that can follow subsequent reactions to form HOM.

Table S5. Reaction barriers of different isomerization reactions of $PhC(O)O_2$.

$PhC(O)O_2$ isomerization	**Reaction barrier (kcal/mol)**†
5-member Endo	25.3
6-member Endo	73.2
7-member Endo	76.4
1,5-Hshift	33.2
1,6-Hshift	113.4
1,7-Hshift	111.0

† Calculated at ωB97X-D/6-31+G* level of theory.

S8. D_2O experiments

In the aromatic carbonyl OH oxidation experiments in presence of D_2O, a near complete H/D exchange was achieved which was monitored by the shift of $HNO_3NO_3^-$ and $(HNO_3)_2NO_3^-$ signals by one and two mass unit, respectively on the mass spectrum (see Figure S5).

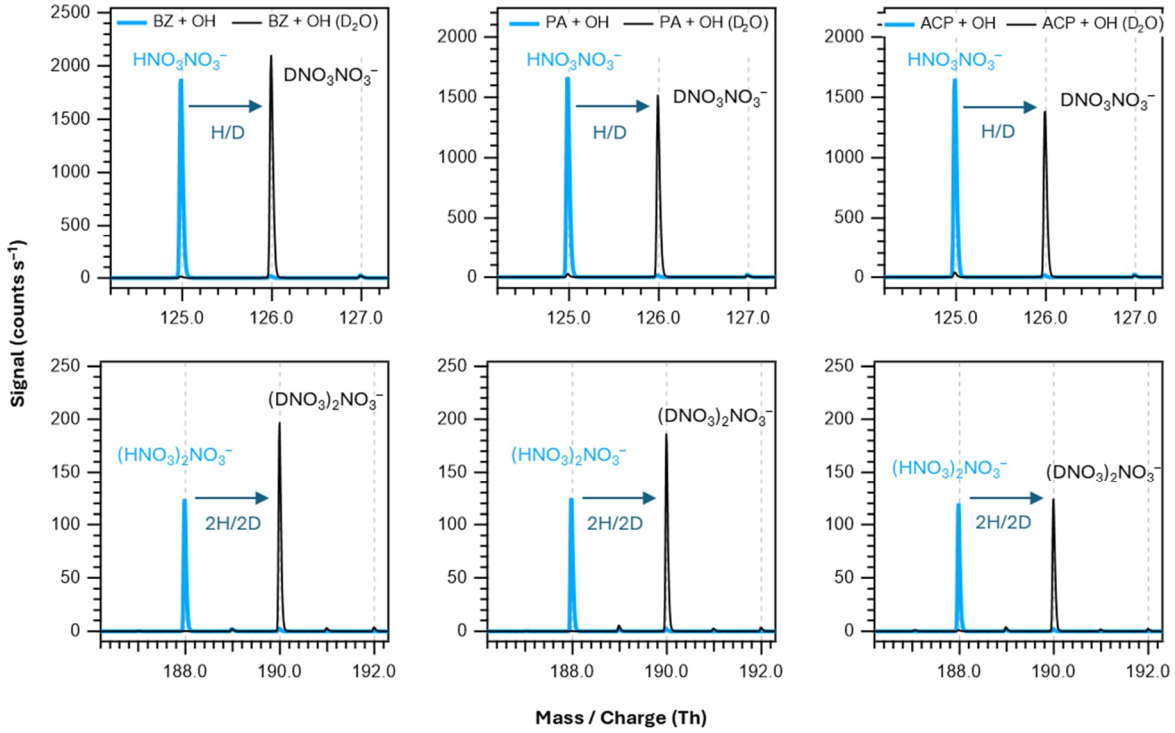

Figure S5. H/D exchange in the reagent ion $HNO_3NO_3^-$ converting it to $DNO_3NO_3^-$ during different aromatic carbonyl OH oxidation reaction in presence of D_2O. BZ = benzaldehyde, PA= phenylacetaldehyde, and ACP = acetophenone.

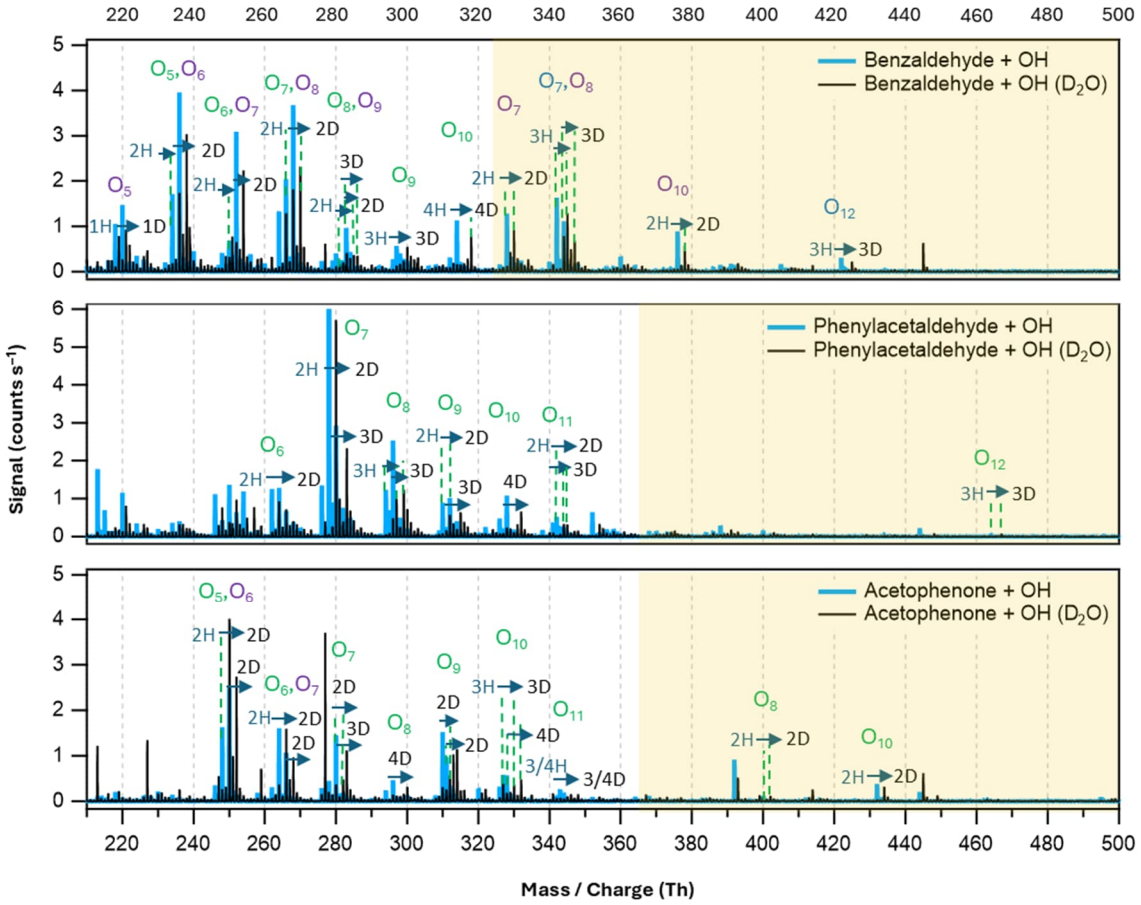

Figure S6. Overlaid nitrate chemical ionization mass spectra of OH initiated oxidation of aromatic carbonyls without (in blue) and with the presence of D_2O (in black). The peak mass shifts during D_2O addition illustrate the number of exchangeable H-atoms present in the product molecular structures. The accretion products are highlighted in light brown background. The labels in green indicate non-fragmented (C_x) products with different number of oxygen atoms while the labels in purple indicate fragmented (C_{x-1}) products. The blue labels (O_7 and O_{12}) in the accretion product region of benzaldehyde spectrum (top panel) indicate products with 13 C atoms (i.e., C_7-RO_2 + C_6-RO_2).

S9. Mechanistic exploration for predicting molecular structures

In this section, we show the additional mechanisms extended from Figure 5 in the main manuscript to predict the molecular structures of the oxidation products supported by the H/D exchange experiments in presence of D_2O. We use the predicted structures of the oxidation products to calculate their volatility discussed in the main manuscript and Section S10 below. Although other alternative pathways are likely available, here we explore those mainly arising from the i-BPR and the subsequent ring-opened peroxy radical. Besides, the alternative autoxidation pathways that can agree with the H/D exchange experiments are likely to produce similar product structures with the same number of OH/OOH groups. Therefore, they will not

significantly alter the current volatility estimation by group additivity and volatility basis set based methods even though the spatial arrangements of the actual isomeric structures could be different.

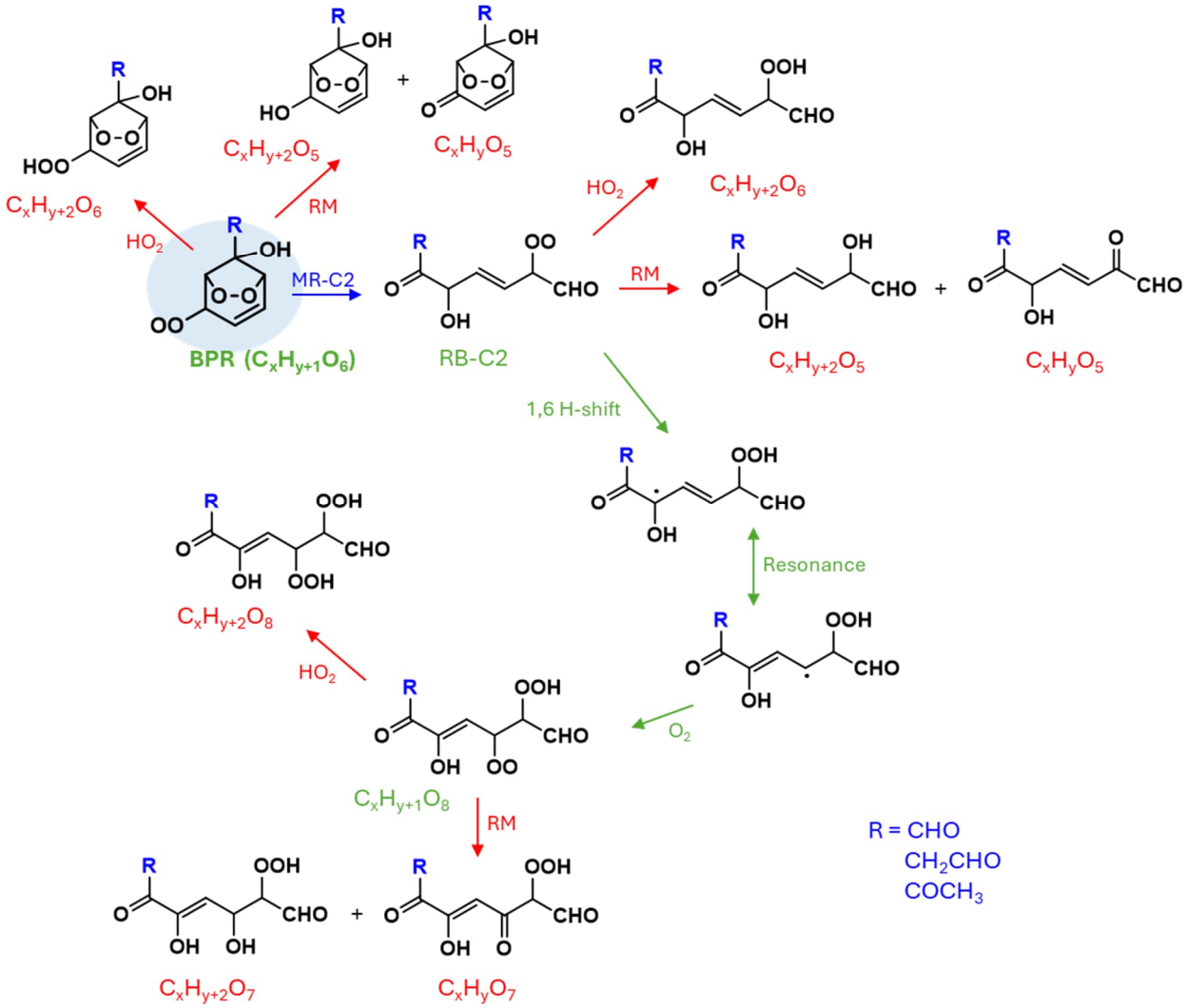

Figure S7. Potential formation pathways of $C_xH_yO_{5,7}$, $C_xH_{y+2}O_{5,7}$, $C_xH_{y+2}O_{6,8}$, and $C_xH_{y+1}O_8$ from bicyclic peroxy radical (BPR, $C_xH_{y+1}O_6$). The green arrows indicate chain propagation reactions while the red arrows indicate chain termination reactions. MR-C2 = molecular rearrangement via C2 channel. RM = Russell mechanism ($RO_2 + R'O_2 \rightarrow ROH + R'_{-H}C{=}O + O_2$).

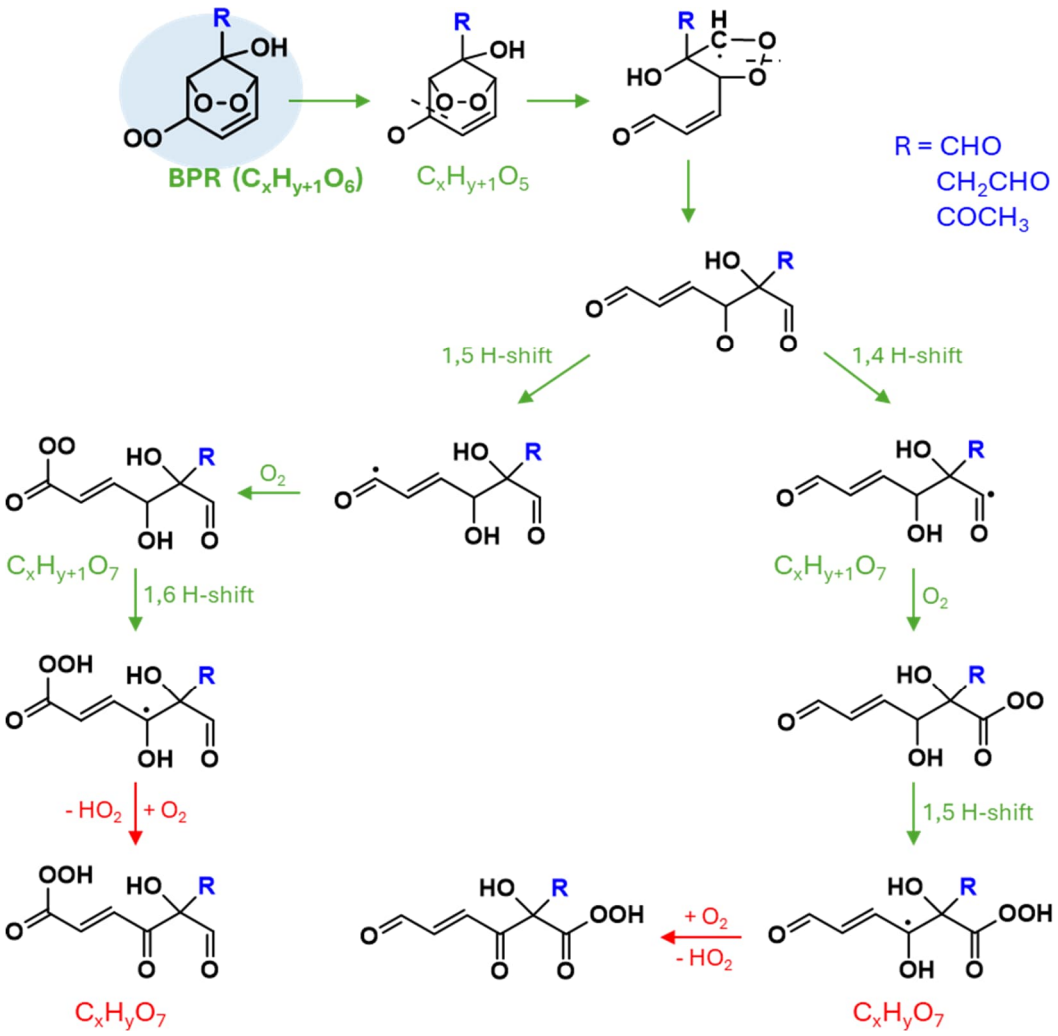

174

175 Figure S8. Potential formation pathways of $C_xH_{y+1}O_7$, and $C_xH_yO_7$ from bicyclic peroxy radical
176 (BPR, $C_xH_{y+1}O_6$) via bicyclic alkoxy radical $C_xH_{y+1}O_5$. The green arrows indicate chain
177 propagation reactions while the red arrows indicate chain termination reactions.

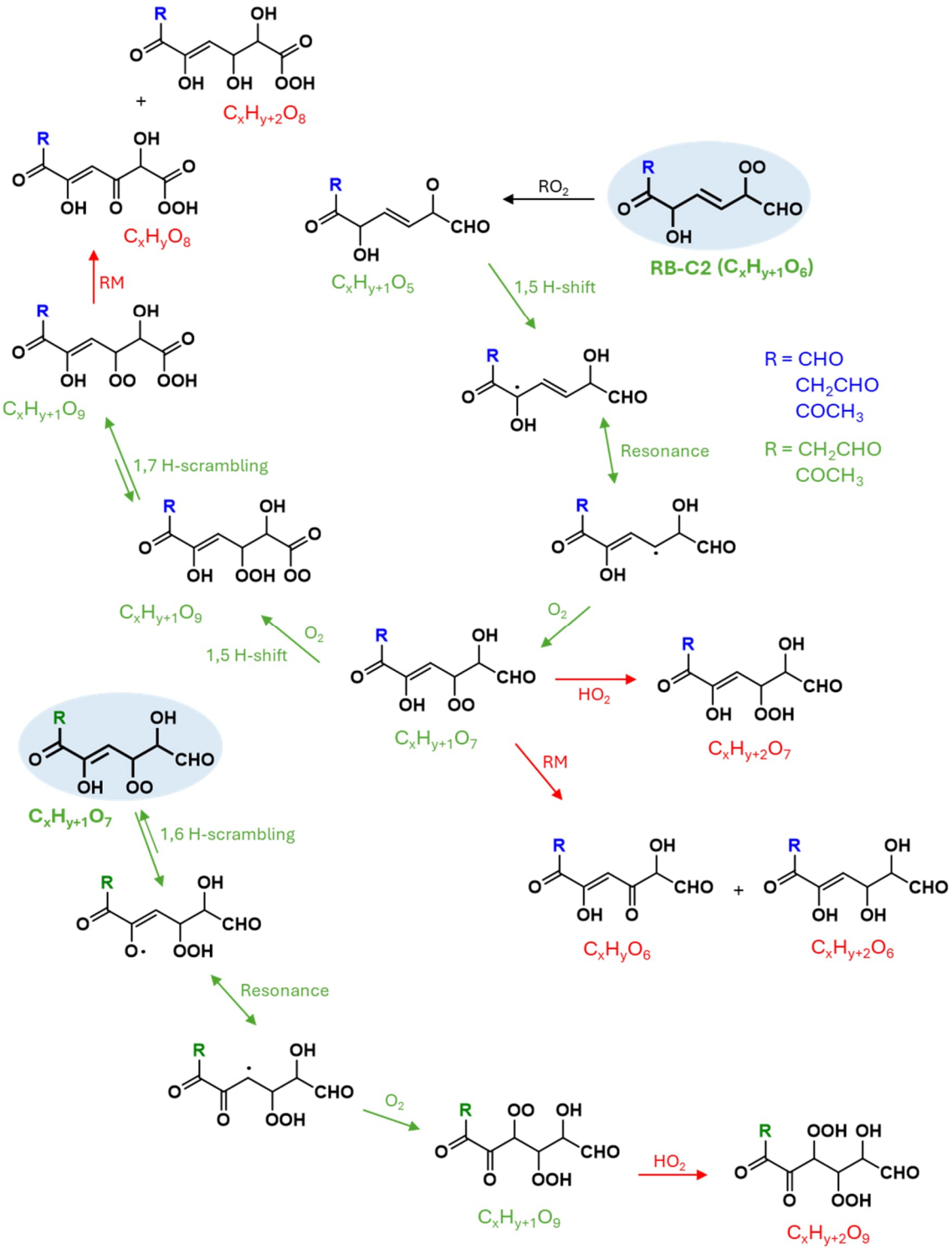

Figure S9. Potential formation pathways of $C_xH_{y+1}O_{7,9}$, $C_xH_yO_{6,8}$, and $C_xH_{y+2}O_{6–9}$ from RB-C2 ($C_xH_{y+1}O_6$). The green arrows indicate chain propagation reactions while the red arrows indicate chain termination reactions. RM = Russell mechanism ($RO_2 + R'O_2 \rightarrow ROH + R'_{-H}C=O + O_2$).

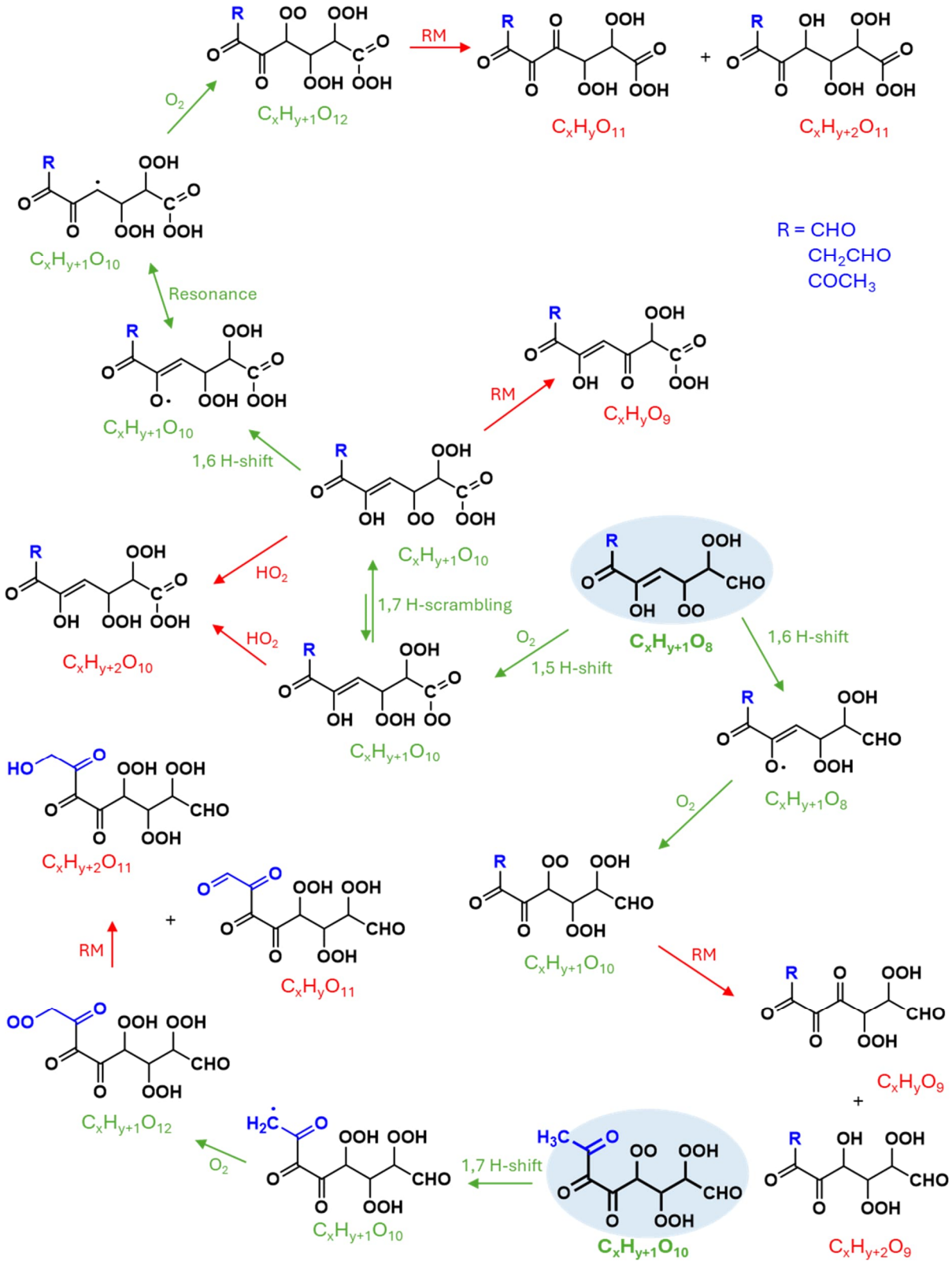

183

184 Figure S10. Potential formation pathways of $C_xH_yO_{9,11}$, $C_xH_{y+2}O_{9,11}$, $C_xH_{y+1}O_{10,12}$, and
185 $C_xH_{y+2}O_{10}$ from O_8 peroxy radical ($C_xH_{y+1}O_8$). The green arrows indicate chain propagation
186 reactions while the red arrows indicate chain termination reactions. RM = Russell mechanism
187 ($RO_2 + R'O_2 \rightarrow ROH + R'_{-H}C{=}O + O_2$). Note that the $C_xH_{y+1}O_{12}$ peroxy radicals reacts also

with HO_2 to form closed shell $C_xH_{y+2}O_{12}$ ($RO_2 + HO_2 \rightarrow ROOH + O_2$) with one more OOH functional group.

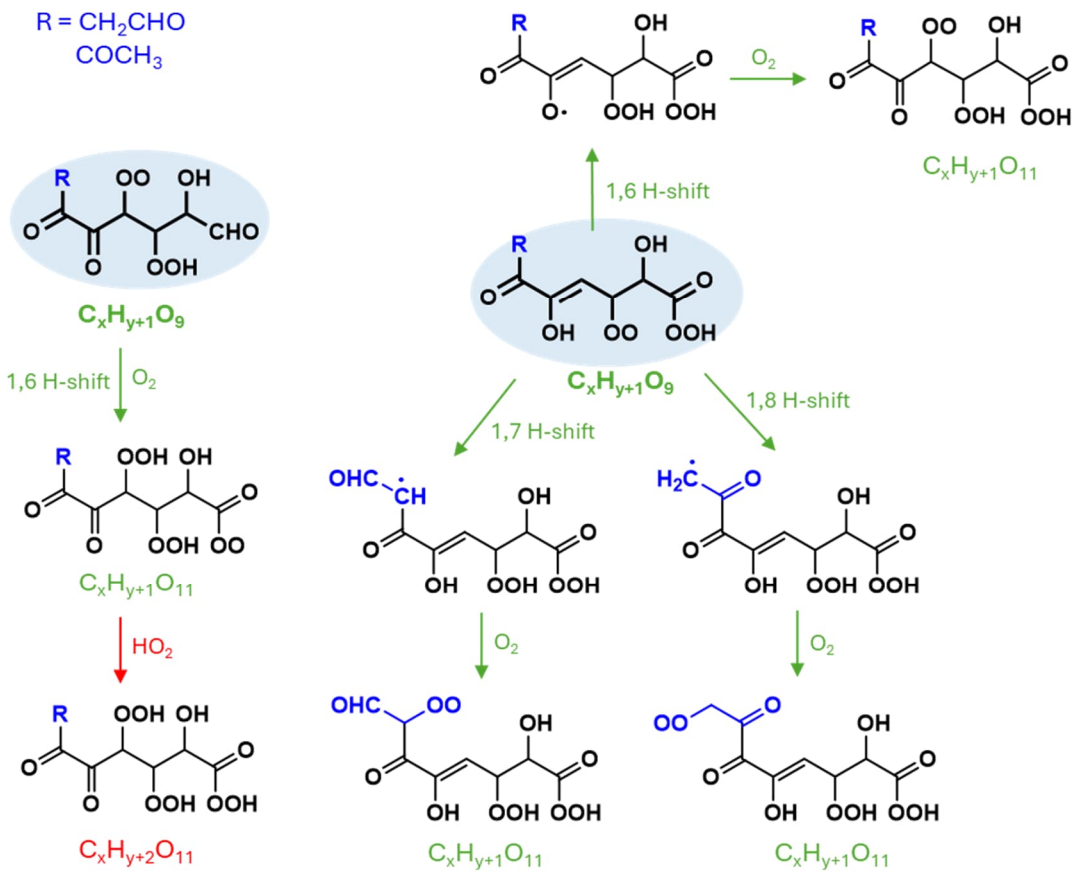

Figure S11. Potential formation pathways of $C_xH_{y+1}O_{11}$, and $C_xH_{y+2}O_{11}$ from O_9 peroxy radical ($C_xH_{y+1}O_9$, see Figure S9) in phenylacetaldehyde and acetophenone oxidation. The green arrows indicate chain propagation reactions while the red arrows indicate chain termination reactions.

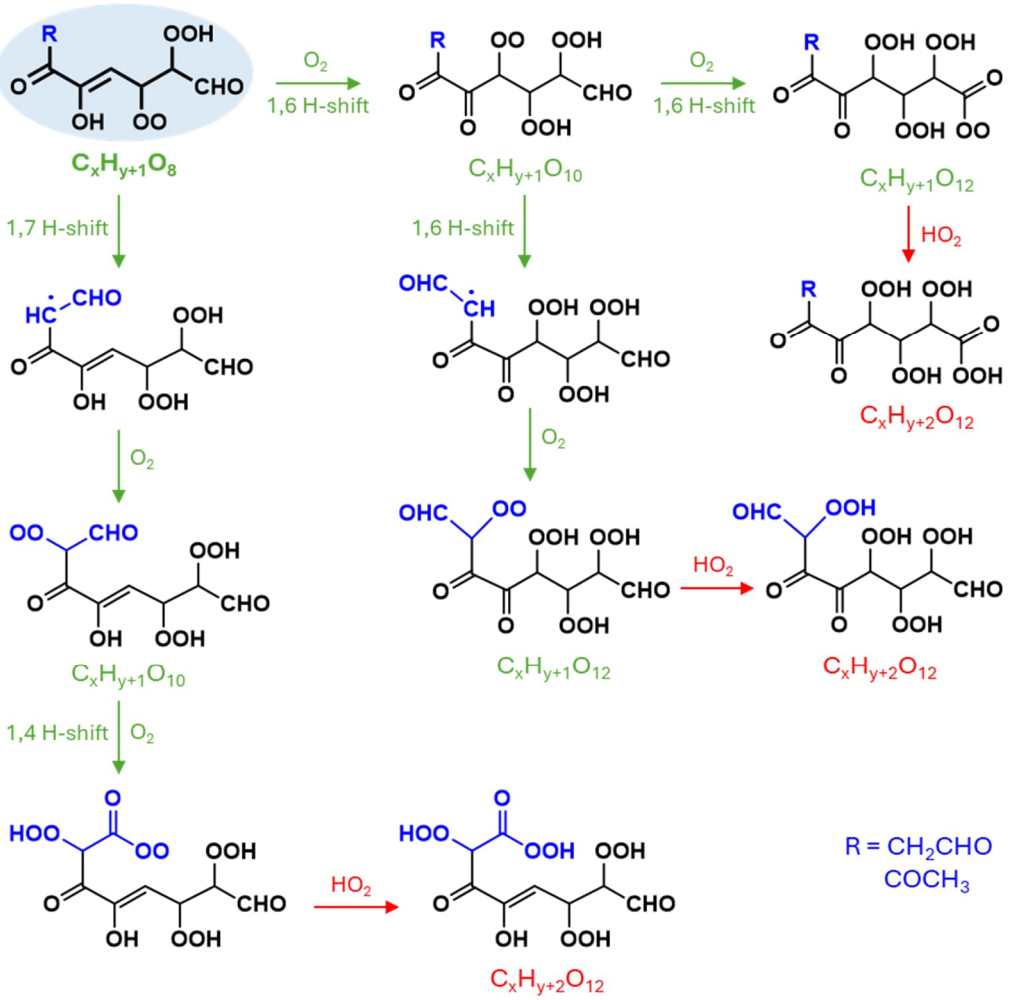

Figure S12. Additional potential pathways of formation of $C_xH_{y+1}O_{12}$, and $C_xH_{y+2}O_{12}$ from O_8 peroxy radical ($C_xH_{y+1}O_8$, see Figure S10) in phenylacetaldehyde and acetophenone oxidation. The green arrows indicate chain propagation reactions while the red arrows indicate chain termination reactions.

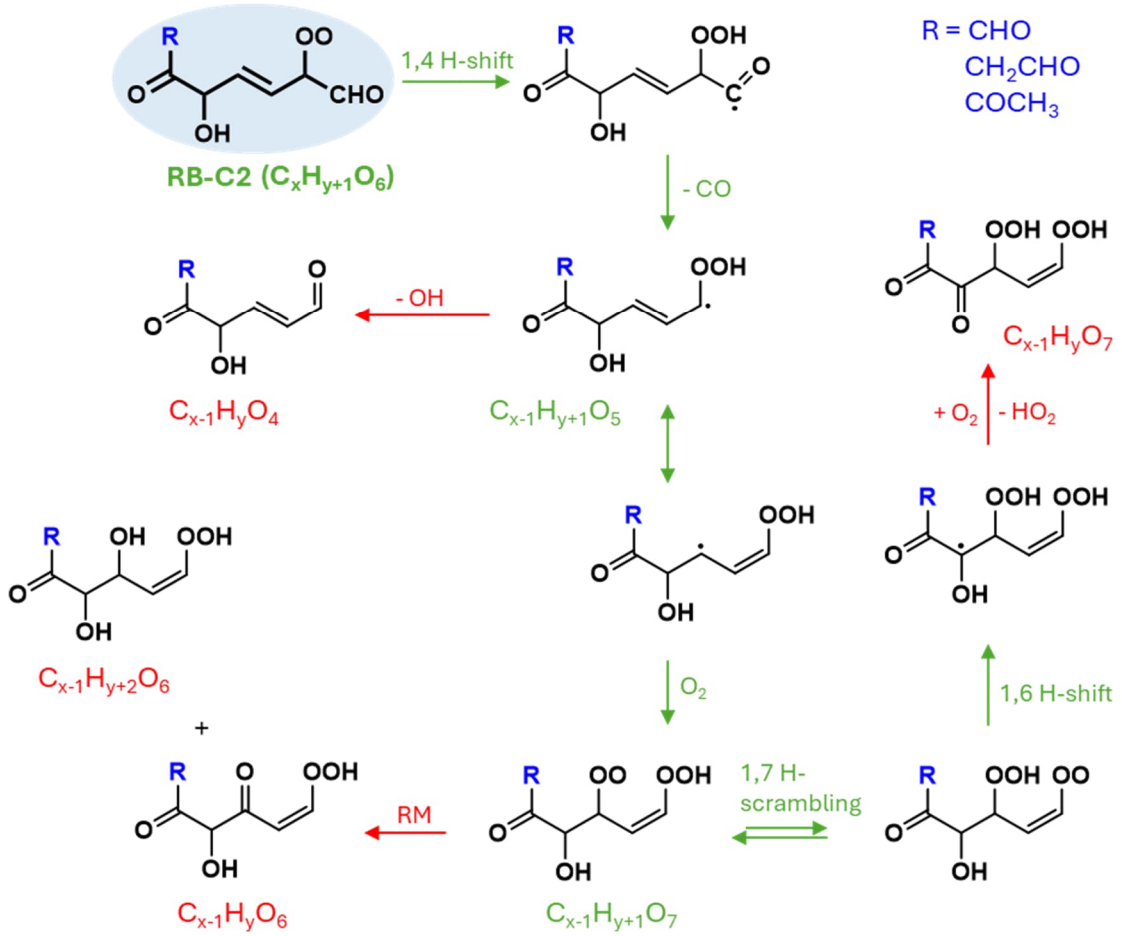

Figure S13. Potential formation pathways of $C_{x-1}H_yO_{6,7}$ from peroxy radical RB-C2 ($C_xH_{y+1}O_6$). The green arrows indicate chain propagation reactions while the red arrows indicate chain termination reactions. RM = Russel mechanism ($RO_2 + R'O_2 \rightarrow ROH + R'_{-H}C=O + O_2$).

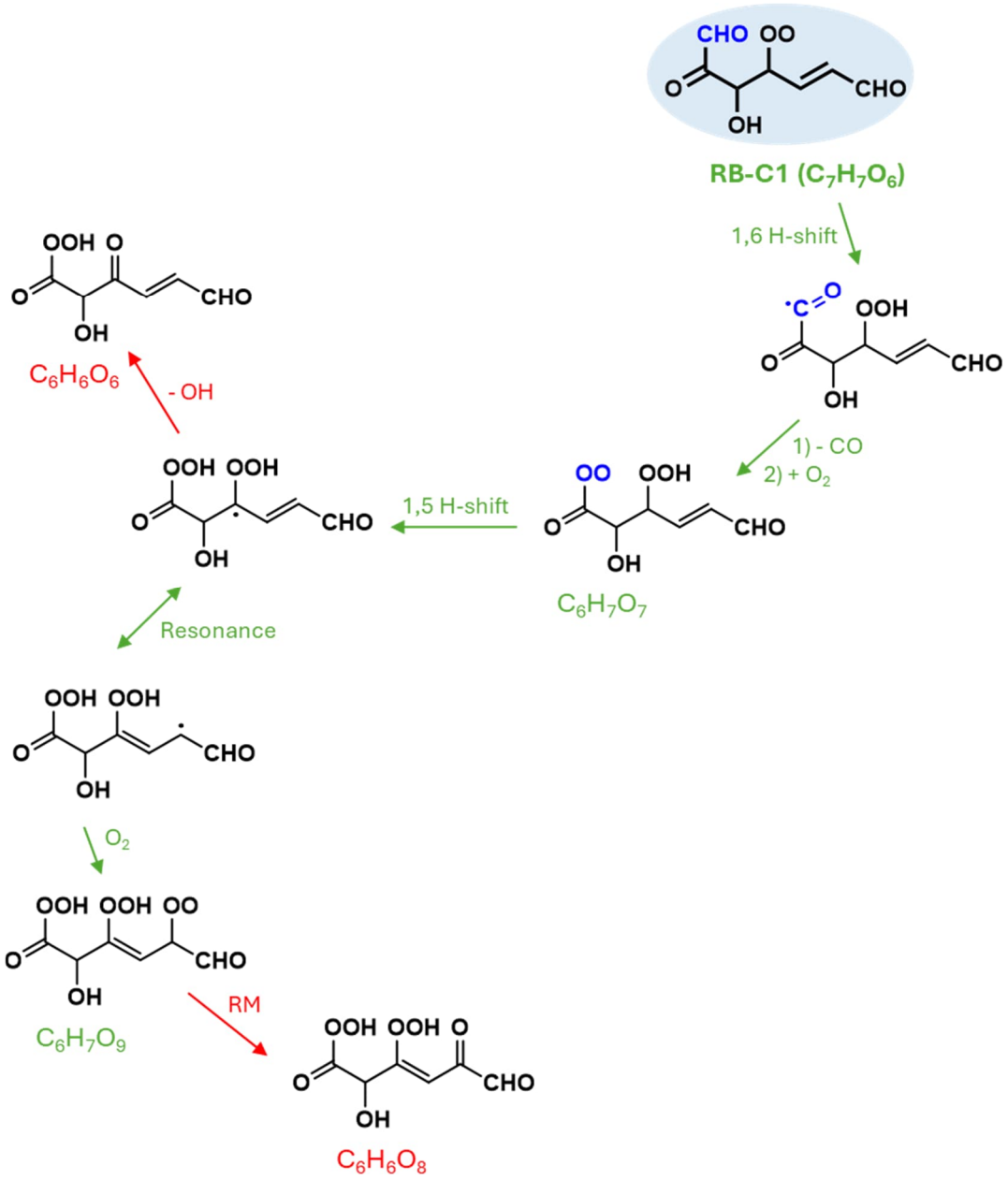

206

207 Figure S14. Potential formation pathways of $C_6H_6O_{6,8}$ from peroxy radical RB-C1 ($C_7H_7O_6$) in
208 benzaldehyde oxidation. The green arrows indicate chain propagation reactions while the red
209 arrows indicate chain termination reactions. RM = Russel mechanism ($RO_2 + R'O_2 \rightarrow ROH +$
210 $R'_{-H}C=O + O_2$).

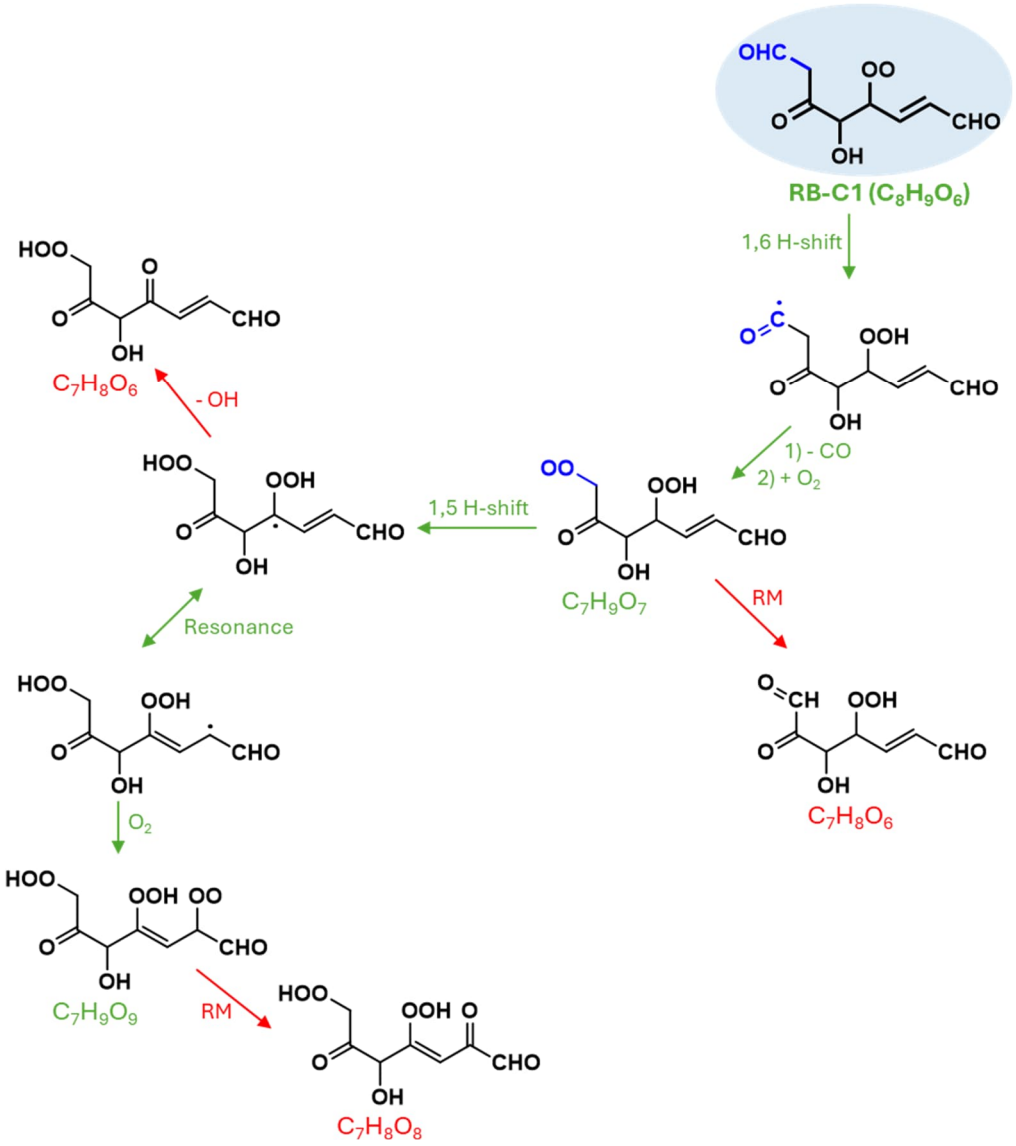

211

212 Figure S15. Potential formation pathways of $C_7H_8O_{6,8}$ from peroxy radical RB-C1 ($C_8H_9O_6$) in
213 phenylacetaldehyde oxidation. The green arrows indicate chain propagation reactions while the
214 red arrows indicate chain termination reactions. RM = Russel mechanism ($RO_2 + R'O_2 \rightarrow ROH$
215 $+ R'_{-H}C=O + O_2$).

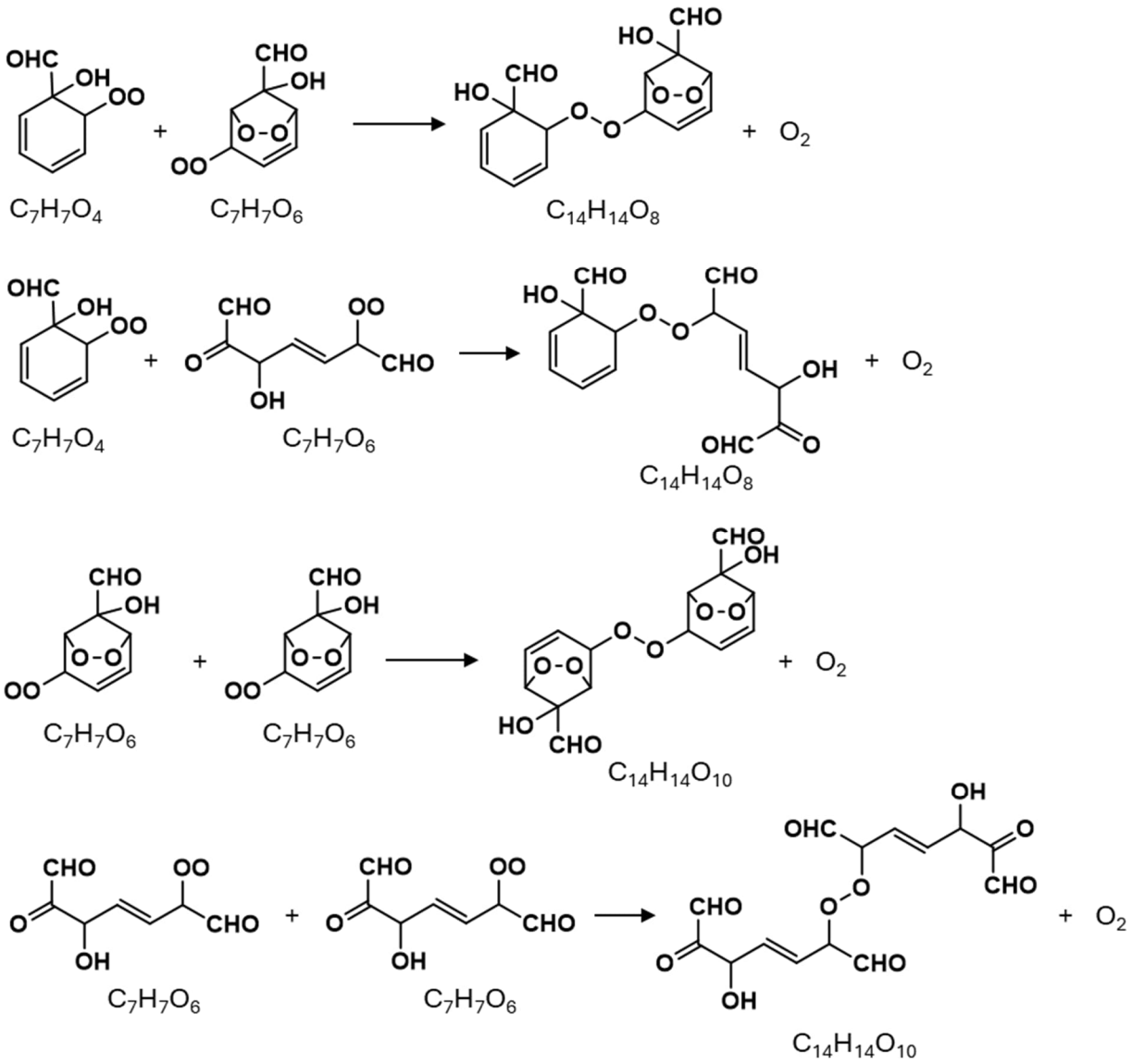

Figure S16. Potential pathways of forming accretion products ($C_{14}H_{14}O_{8,10}$) by different combinations of monomeric alkyl peroxy (RO_2) radicals (i.e., $RO_2 + R'O_2 = (ROOR' + O_2)$ in benzaldehyde OH oxidation.

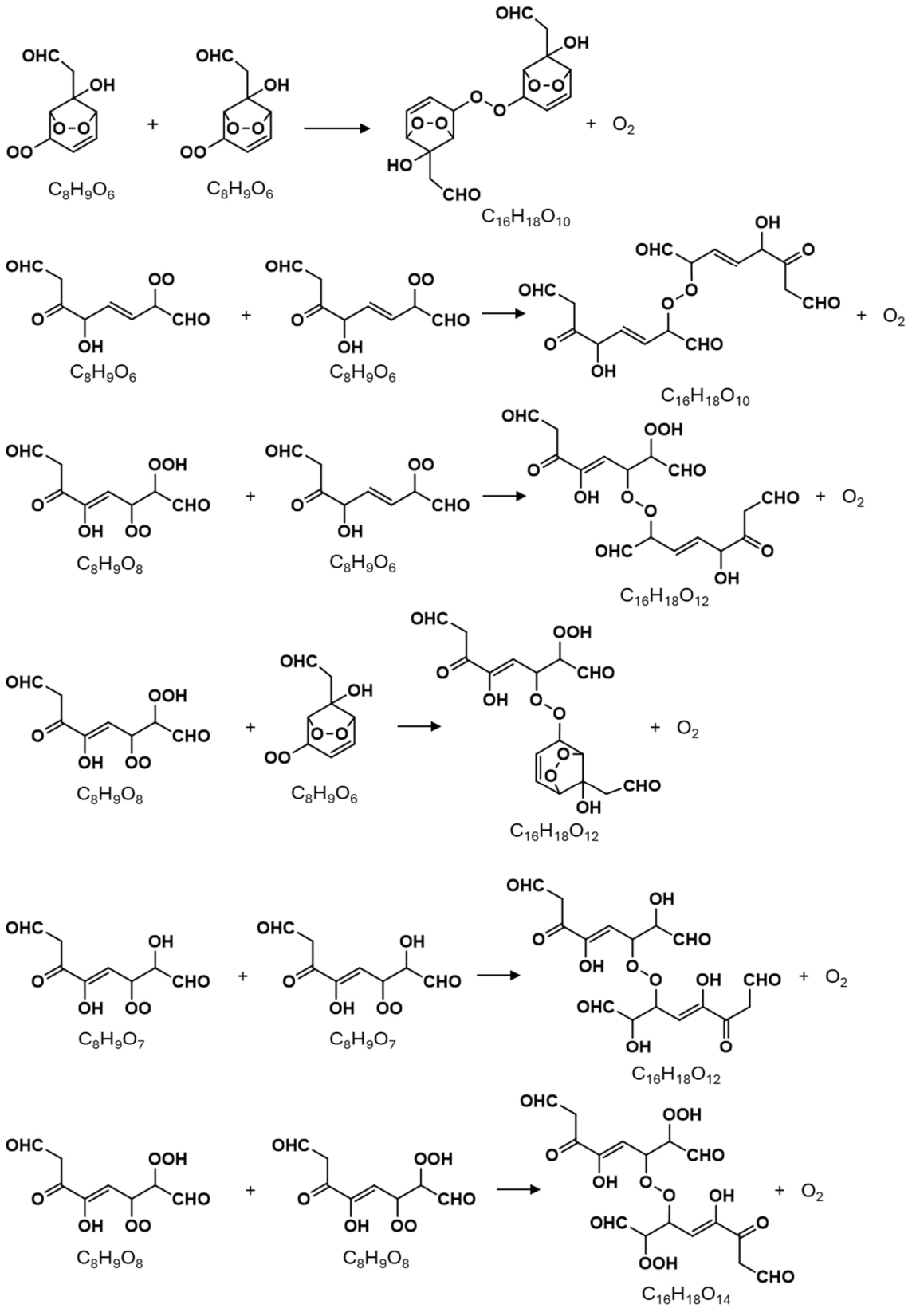

Figure S17. Potential formation pathways of accretion products ($C_{16}H_{18}O_{10,12,14}$) by different combinations of monomeric alkyl peroxy (RO_2) radicals (i.e., $RO_2 + R'O_2 = (ROOR' + O_2)$ in phenylacetaldehyde OH oxidation.

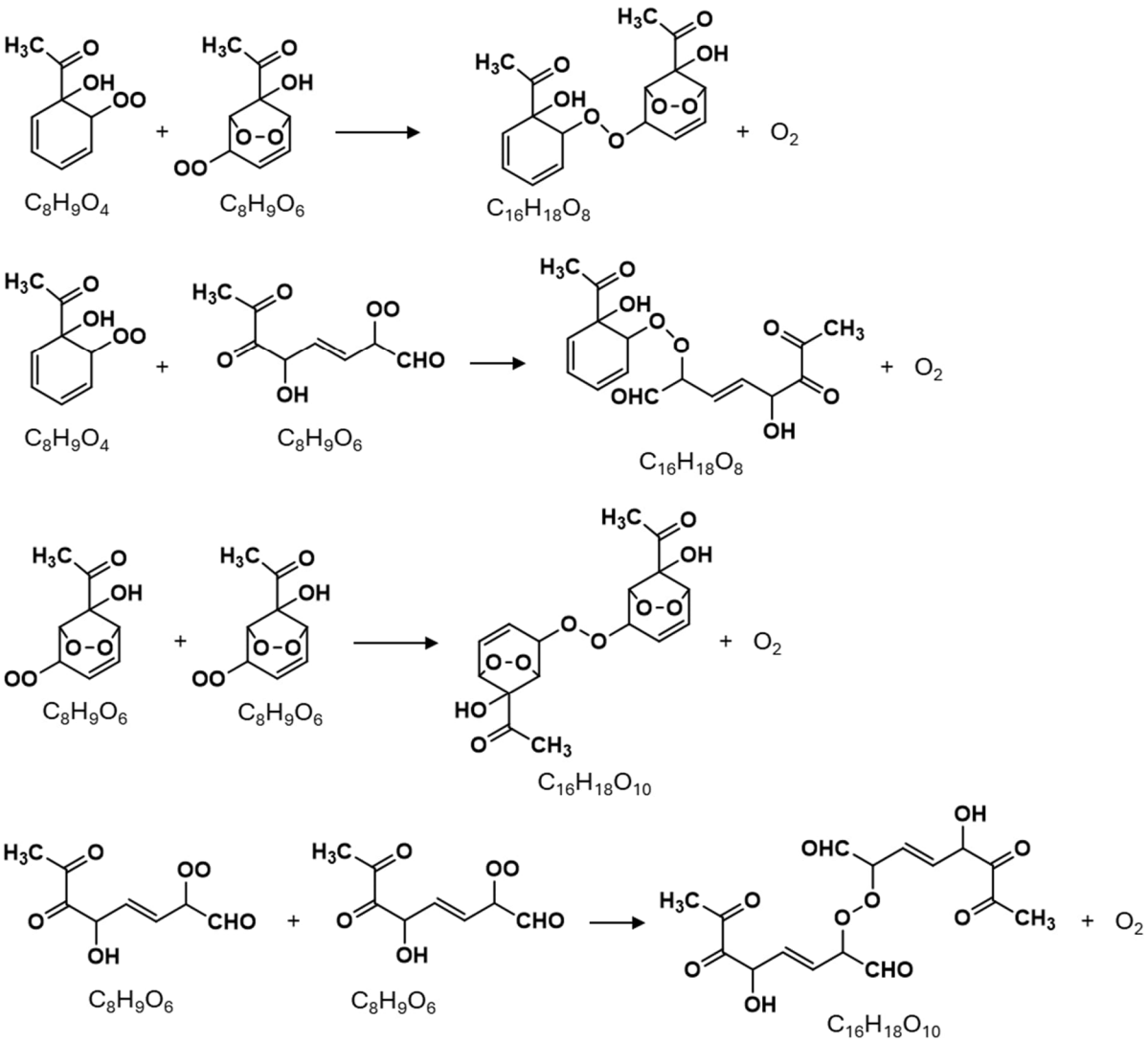

Figure S18. Potential formation pathways of accretion products ($C_{16}H_{18}O_{8–10}$) by different combinations of monomeric alkyl peroxy (RO_2) radicals (i.e., $RO_2 + R'O_2 = (ROOR' + O_2)$ in acetophenone OH oxidation.

S10. Volatility classification and regression analysis details

This section provides additional details on the prediction of vapor concentration of products (experiments in the presence of NO) and their classification across different volatility classes provided in Figure 6 in the main manuscript. The oxidation products of phenylacetaldehyde, benzaldehyde, and acetophenone are categorized into volatility classes based on their predicted vapor concentrations, determined by averaging the results of six models: Nanoolal,[5] EVAP,[6] Myrdal-Yalkowsky,[7] SIMPOL,[8] Stolzenburg,[9] and Mohr.[10]

The scatter plots (see Figure S19) illustrate the relationship between saturation vapor concentration and molar mass (MM) for the compounds, as estimated using six vapor pressure prediction models. The averaged values represent the average of these six predictions. Linear

regression analyses were performed for the whole data of the six models (dashed black line) as well as exclusively for the averaged values (solid black line), demonstrating a clear correlation. These findings highlight the different vapor pressure trends based on different models while also emphasizing variations among individual estimates. Figure S20 presents pie charts illustrating the percentage distribution of the number of oxidation products across different volatility classes categorized based on their saturation mass concentration, C^* (μg m^{-3}), including ultra-low VOC (ULVOC, $C^* \leq 10^{-9}$ μg m^{-3}), extremely-low VOC (ELVOC, $10^{-9} < C^* \leq 10^{-5}$ μg m^{-3}), low VOC (LVOC, $10^{-5} < C^* \leq 10^{-1}$ μg m^{-3}), semi VOC (SVOC, $10^{-1} < C^* \leq 10^{2}$ μg m^{-3}), intermediate VOC (IVOC, $10^{2} < C^* \leq 10^{6}$ μg m^{-3}).[9]

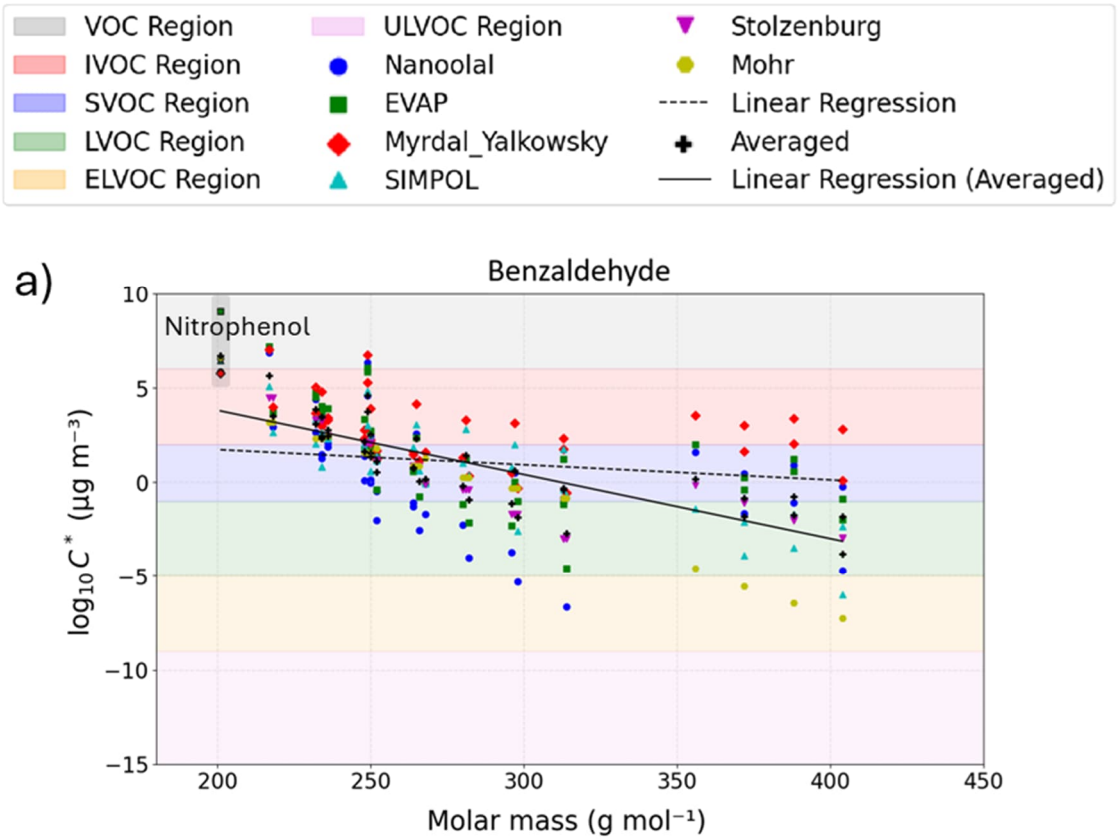

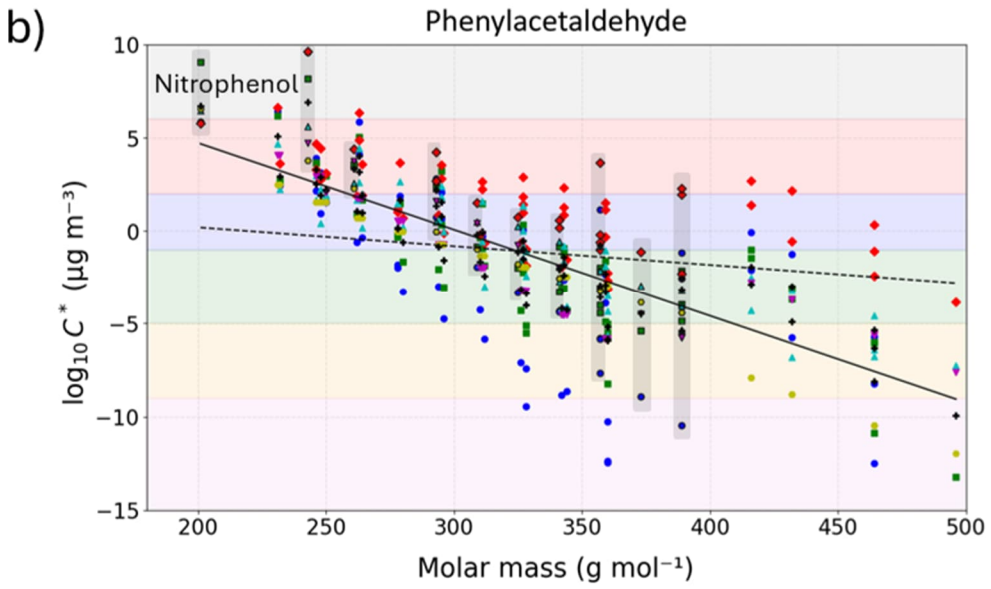

248

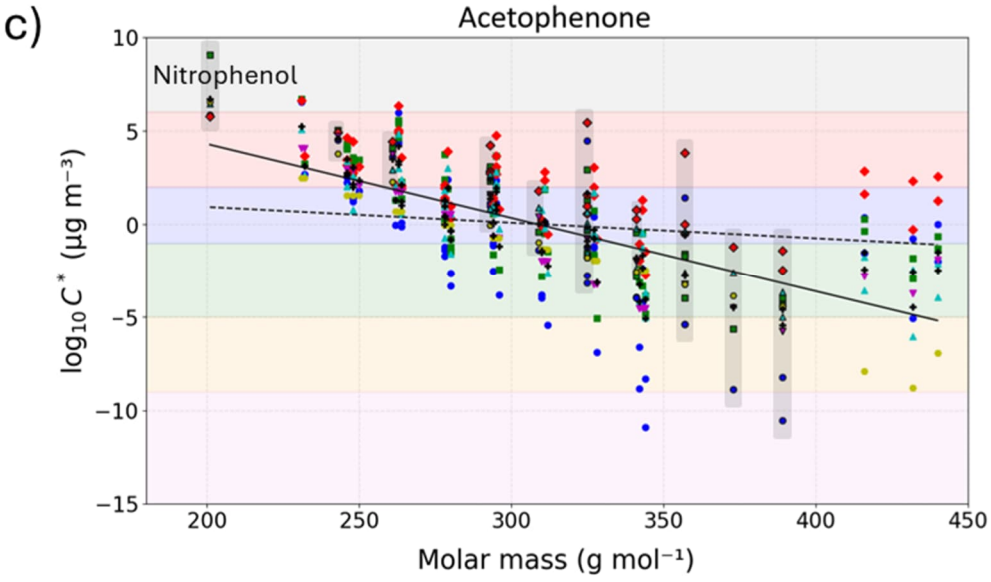

249

250 Figure S19. The relationship between molar mass and $\log_{10}C^*$ estimated using six vapor
251 pressure prediction models. Different markers represent individual models, while nitrogen-
252 containing compounds (mostly organonitrates except the nitrophenol) are highlighted with
253 black borders within grey columns.

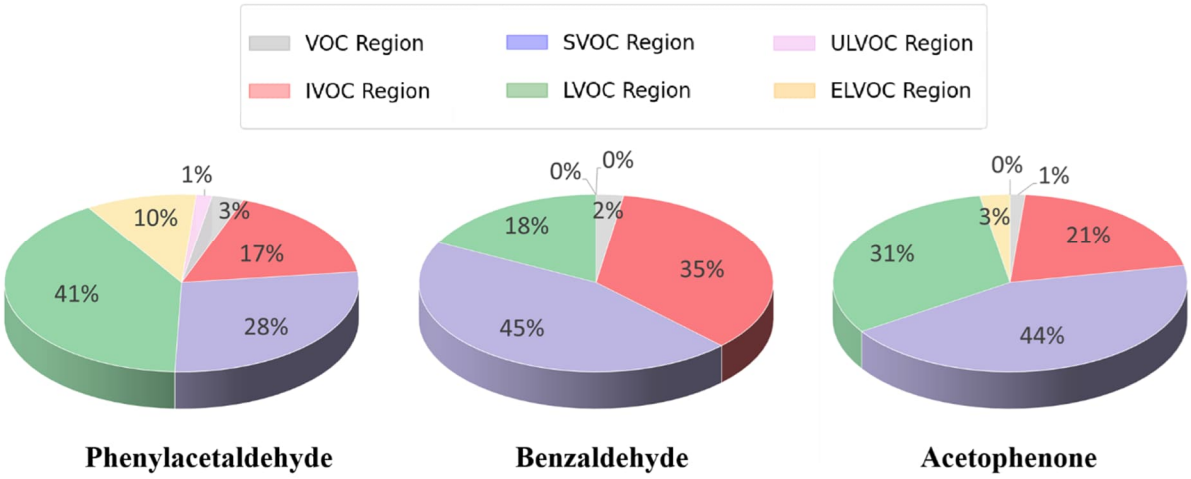

Figure S20. Volatility classification of oxidation products from phenylacetaldehyde, benzaldehyde, and acetophenone (in the presence of NO). The classifications are based on the averaged vapor concentration predictions from six models: Nanoolal, EVAP, Myrdal-Yalkowsky, SIMPOL, Stolzenburg, and Mohr. The pie charts illustrate the percentage distribution of oxidation products across six volatility classes (ULVOC, ELVOC, LVOC, SVOC, IVOC, and VOC), determined using the averaged predictions from these models.

The correlation of the linear regression lines for the total dataset from all six models (dashed black line) and the averaged dataset (solid black line), as shown in Figure S19, is presented in Table S6. The root mean square error (RMSE) values for both lines are calculated based on the entire dataset, meaning that for the solid black line derived from the averaged dataset, its RMSE is determined using all individual data points rather than the averaged values. Additionally, Table S7 reports the RMS difference for each individual model (Nanoolal, EVAP, Myrdal-Yalkowsky, SIMPOL, Stolzenburg, and Mohr), representing the deviation of each model's predictions from the averaged linear regression line. These values quantify how much each model deviates from the overall trend predicted by the combined model set.

Table S6. Linear regression equations and root mean square error (RMSE) values for vapor concentration predictions of oxidation products from acetophenone, benzaldehyde, and phenylacetaldehyde. The regression is performed using the total dataset from six models (dashed black line) and the averaged dataset (solid black line). RMSE values indicate the overall deviation of predictions from the regression line.

Model	**Linear Regression Formula**	**RMSE ($\mu g\ m^{-3}$)**
Acetophenone (total dataset)	$\log_{10}C^* = -0.0084\ MM + 2.6053$	3.0497
Acetophenone (averaged dataset)	$\log_{10}C^* = -0.0395\ MM + 12.1966$	1.4850

Benzaldehyde (total dataset)	$\log_{10}C^* = -0.0080\ MM + 3.3261$	2.7469
Benzaldehyde (averaged dataset)	$\log_{10}C^* = -0.0340\ MM + 10.6084$	1.2990
Phenylacetaldehyde (total dataset)	$\log_{10}C^* = -0.0101\ MM + 2.2131$	3.8112
Phenylacetaldehyde (averaged dataset)	$\log_{10}C^* = -0.0465\ MM + 14.0257$	1.5165

† MM = molar mass.

Table S7. Root mean square (RMS) difference (μg m^{-3}) between individual model predictions (Nanoolal, EVAP, Myrdal-Yalkowsky, SIMPOL, Stolzenburg, and Mohr) and the averaged linear regression line for acetophenone, benzaldehyde, and phenylacetaldehyde. These values represent the extent to which each model deviates from the mean behavior across all models.

Model	**Acetophenone**	**Benzaldehyde**	**Phenylacetaldehyde**
Nanoolal	3.3433	2.7554	3.8556
EVAP	2.1908	2.2599	2.2300
Myrdal-Yalkowsky	2.7918	2.5636	3.4101
SIMPOL	1.4839	1.3361	1.4573
Stolzenburg	1.6269	1.3242	1.7134
Mohr	1.4483	1.7116	1.2121

S11. Kinetic simulation

S11.1 Simulations without and with NO

Chemical kinetic simulations are carried out using Kinetiscope Program[11,12] to estimate the concentrations of oxidant OH and primary RO_2 radicals in different aromatic carbonyl oxidation reactions without (reaction steps 1–3 below) and with the presence of NO (reaction steps 1–12 below). We use an experimental rate coefficient of 1.2×10^{-11} cm^3 $molecule^{-1}$ s^{-1} for benzaldehyde (BZ) + OH reaction.[13] For the reactions of phenylacetaldehyde (PA) + OH and acetophenone (ACP) + OH, we do not find experimental rate coefficients in the literature and hence use SAR predicted rate coefficients of 4.19×10^{-11} and 3.86×10^{-12} cm^3 $molecule^{-1}$ s^{-1}, respectively for these reactions (see Tables S2–3 in Section S3). In our flow reactor setup, we produce OH radicals in situ by the ozonolysis reaction of tetramethyl ethylene (TME). The produced OH radicals react with TME as well as with the aromatic carbonyl in the flow reactor. In the simulations, we use reaction rate coefficients k_{TME-O_3} of 1.5×10^{-15} and k_{TME-OH} of 1.0×10^{-10} cm^3 $molecule^{-1}$ s^{-1} accounting for the corresponding reactions.[14] As initial precursor concentrations, 1 ppm (2.46×10^{13} molecules cm^{-3}) of VOC, 52–109 ppb ($1.28–2.68 \times 10^{12}$ molecules cm^{-3}) of TME, and 263–318 ppb ($6.47–7.82 \times 10^{12}$ molecules cm^{-3}) of ozone, identical to the experimental conditions, are used (see Table 1 of the main manuscript for details). In the flow reactor experiments, high VOC concentrations were used

to scavenge OH, especially as TME reacts so fast with it. Following the reaction of aromatic carbonyl with OH, the initially formed carbon centered radical readily undergoes a pseudo unimolecular reaction with O_2 to form a primary RO_2 radical. For simplification, we show the formation of different RO_2 radicals directly from the reactions of aromatic carbonyl with OH, and TME with OH. Here, TME produced RO_2 and aromatic carbonyl produced RO_2 are separated by the expressions RO_2_T and RO_2_C respectively.

With the addition of NO in the reaction system, it is expected to influence the concentrations of OH radicals and primary RO_2 radicals. Therefore, to simulate the experiments with NO, we include the bimolecular reaction rate coefficients of $k_{NO-OH} = 3.3 \times 10^{-11}$, $k_{HONO-OH} = 6.0 \times 10^{-12}$, $k_{NO-O_3} = 1.8 \times 10^{-14}$, and $k_{NO_2-OH} = 4.1 \times 10^{-11}$ cm^3 molecule^{-1} s^{-1},[15] with respect to their corresponding reactions in the simulation. Besides, bimolecular rate coefficients for RO_2 + RO_2 and RO_2 + NO reactions are set to the generic values of 3.2×10^{-11} and 9.0×10^{-12} cm^3 molecule^{-1} s^{-1}, respectively[16,17] to account for sinks of RO_2 radicals. The influences of NO + HO_2 and RO_2 + NO_2 reactions on OH and RO_2_C radical concentrations are examined separately and discussed in the section below. An example of the reaction steps used in the current simulation is as follows. The results are shown in Figure S21 and Table S8.

1. TME + O_3 => OH ($k_{TME-O_3} = 1.5 \times 10^{-15}$ cm^3 molecule^{-1} s^{-1})
2. TME + OH => RO_2_T ($k_{TME-OH} = 1.0 \times 10^{-10}$ cm^3 molecule^{-1} s^{-1})
3. PA + OH => RO_2_C ($k_{PA-OH} = 4.24 \times 10^{-11}$ cm^3 molecule^{-1} s^{-1})
4. NO + OH => HONO ($k_{NO-OH} = 3.3 \times 10^{-11}$ cm^3 molecule^{-1} s^{-1})
5. HONO + OH => H_2O + NO_2 ($k_{HONO-OH} = 6.0 \times 10^{-12}$ cm^3 molecule^{-1} s^{-1})
6. NO + O_3 => NO_2 + O_2 ($k_{NO-O_3} = 1.8 \times 10^{-14}$ cm^3 molecule^{-1} s^{-1})
7. NO_2 + OH => HNO_3 ($k_{NO_2-OH} = 4.1 \times 10^{-11}$ cm^3 molecule^{-1} s^{-1})
8. 2 RO_2_T => Sink_a ($k_{RO_2-RO_2} = 3.2 \times 10^{-11}$ cm^3 molecule^{-1} s^{-1})
9. 2 RO_2_C => Sink_b ($k_{RO_2-RO_2} = 3.2 \times 10^{-11}$ cm^3 molecule^{-1} s^{-1})
10. RO_2_T + RO_2_C => Sink_ab ($k_{RO_2-RO_2} = 3.2 \times 10^{-11}$ cm^3 molecule^{-1} s^{-1})
11. RO_2_T + NO => $RONO_2$ ($k_{RO_2-NO} = 9.0 \times 10^{-12}$ cm^3 molecule^{-1} s^{-1})
12. RO_2_C + NO => $RONO_2$ ($k_{RO_2-NO} = 9.0 \times 10^{-12}$ cm^3 molecule^{-1} s^{-1})

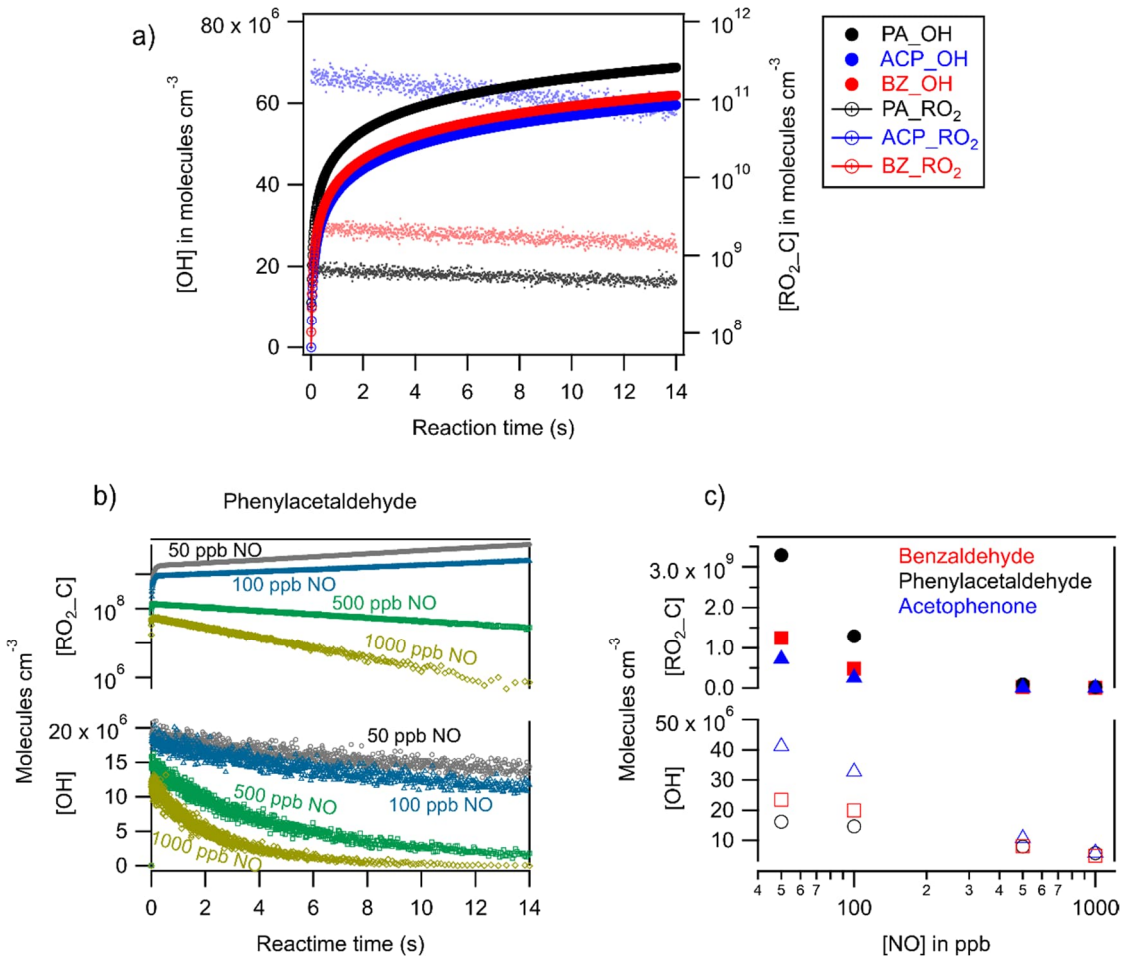

Figure S21. Concentration profiles of OH and primary RO_2_C radicals produced in aromatic carbonyl oxidation derived by chemical kinetic simulations under laboratory flow reactor experimental condition without NO (a) and with NO (b–c). Panel (b) shows results from phenylacetaldehyde. In panel (c), average concentrations of OH and RO_2_C during 14 s reaction time are presented. PA = phenylacetaldehyde, ACP = acetophenone, and BZ = benzaldehyde.

Figure S21a and Table S8 imply that the average concentrations of oxidant OH and primary RO_2_C radicals in the flow reactor are comparable in different aromatic carbonyl oxidation experiments. In the experiments without NO, the simulation produced average concentrations of OH radicals are 2.75×10^7, 1.77×10^7, and 6.26×10^7 molecules cm^{-3} for the experiments with BZ, PA, and ACP, respectively.

Table S8. Average concentrations of OH and RO_2 radicals produced in different aromatic carbonyl oxidation experiments derived from chemical simulations under laboratory conditions.

Expt. type	Model input				Model output	
(VOC)	**[VOC] ppmv**	**[TME] ppbv**	**[O_3] ppbv**	**[NO] ppbv**	**[OH] #/cm^3**	**[RO_2_C] #/cm^3**
Simulation without NO						
BZ	1	52.4	263	–	2.75×10^7	5.61×10^{10}
PA	1	104.8	263	–	1.77×10^7	1.28×10^{11}
ACP	1	52.4	318	–	6.26×10^7	4.15×10^{10}
In the presence of NO						
BZ	1	52.4	263	50	2.35×10^7	1.25×10^9
				100	2.00×10^7	4.79×10^8
				500	8.11×10^6	2.68×10^7
				1000	4.99×10^6	7.33×10^6
PA	1	104.8	263	50	1.62×10^7	3.29×10^9
				100	1.47×10^7	1.29×10^9
				500	7.99×10^6	9.23×10^7
				1000	5.86×10^6	3.04×10^7
ACP	1	52.4	263	50	4.12×10^7	7.24×10^8
				100	3.28×10^7	2.58×10^8
				500	1.07×10^7	1.15×10^7
				1000	5.90×10^6	2.83×10^6

The corresponding RO_2_C radical concentrations are 5.61×10^{10}, 1.28×10^{11}, and 4.15×10^{10} molecules cm^{-3}, respectively. While the OH concentrations for BZ and PA experiments are closer to each other, it is higher for the ACP experiment by a factor of 2 to 3. This can be attributed to the slower OH reactivity with ACP compared to BZ and PA (see Section S3 above). It is also reflected in the concentrations of primary RO_2_C radical in the three studied systems, with PA yielding the highest RO_2_C concentration as it has the highest reactivity with OH of the three molecules. In the presence of NO, Figure S21b shows how the concentration profiles of OH and RO_2_C radicals evolve in time with PA oxidation experiment as an example. In all the aromatic carbonyl systems studied, the primary RO_2_C radical concentration steadily increases with time under 50 ppb and 100 ppb NO conditions. However, at 500 ppb and 1000 ppb NO conditions, the concentrations of RO_2_C radicals decrease with time soon after achieving their initial peak values. In the case of OH radicals, the concentrations show a general decreasing trend with time while at higher NO conditions, we observe a faster decreasing tendency in concentrations as expected. It is also interesting to see that the higher OH reactivity of PA compared to the other two aromatic carbonyls is reflected even under high NO conditions in terms of the PA-derived primary RO_2_C radical concentration being higher than that of BZ and ACP (see Figure S21c and Table S8).

S2.2 Impact of HO_2 and PAN on OH and RO_2

In the gas-phase oxidation process of volatile organic compounds (VOCs), it is usual to produce hydroperoxy radicals (HO_2) alongside the production of alkyl peroxy radicals (RO_2). In the presence of NO, the HO_2 radicals react with NO to recycle OH and NO_2 radicals in the reaction system (see reaction step 13).[15]

13. HO_2 + NO => OH + NO_2 (k_{HO_2-NO} = 8.91 × 10^{-12} cm^3 $molecule^{-1}$ s^{-1})

In the flow reactor system, we presume that the production of HO_2 radicals is about 30% of total primary RO_2 radicals (RO_2_T + RO_2_C). Therefore, to examine the influence of the HO_2 reaction with NO on the concentrations of OH and RO_2_C radicals, we run a separate set of simulations on Kinetiscope including the reaction step 13. An initial HO_2 concentration of 30% of total RO_2 (e.g., 4.78 × 10^8 molecules cm^{-3} of HO_2 in PA oxidation at 100 ppb NO) obtained from the previous simulation without HO_2 is used in the subsequent simulation. Figure S22a shows the results of PA oxidation process without and with involving the reaction step 13. In all aromatic carbonyl simulations, the reaction step 13 does not seem to alter the average concentrations of OH and RO_2_C radicals given that the reaction scheme (reaction steps 1–13) is lacking a constant source of 30% HO_2.

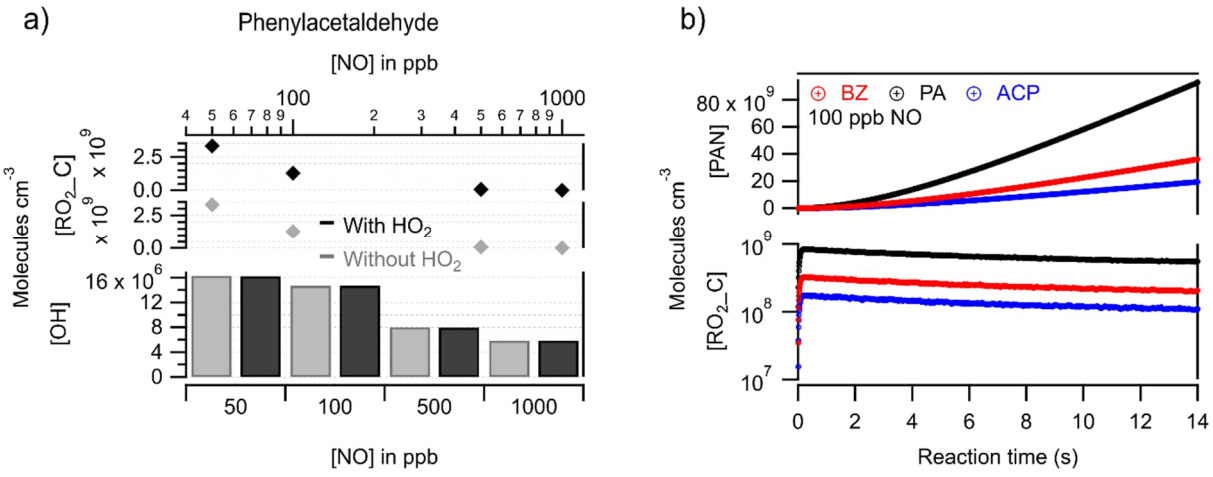

Figure S22. Average concentrations of OH and primary RO_2_C radicals produced in phenylacetaldehyde oxidation derived by chemical kinetic simulations under laboratory conditions with varying NO (a). In panel (a), simulations that include the reaction step HO_2 + NO → OH + NO_2 are presented in black, while simulations without this reaction step are presented in grey. Panel (b) shows the time series of RO_2_C radicals, and maximum possible peroxyacyl nitrate (PAN) concentrations formed in different aromatic carbonyl OH oxidation

reactions. PA = phenylacetaldehyde (black), ACP = acetophenone (blue), and BZ = benzaldehyde (red).

The aromatic carbonyl produced RO_2_C reacts with NO_2 also that is produced in situ in the flow reactor oxidation system according to reaction steps 5 and 6. Here, the reaction of RO_2_C with NO_2 acts as a sink of RO_2_C producing organic nitrates including peroxyacyl nitrates (PAN). We estimate a maximum possible PAN formation by including the reaction step 13' in another separate set of simulations. The idea is to observe to what extent the NO_2 reaction drops the average concentration of RO_2_C limiting its potential to oxidize further to form HOM. Alkyl and acyl peroxy radicals react with NO_2 with rate coefficients of 9.0×10^{-12} and 1.1×10^{-11} cm^3 $molecule^{-1}$ s^{-1}, respectively.[17] Because we cannot differentiate between the two peroxy radicals in a pool of total RO_2_C, an average rate coefficient $k_{RO_2-NO_2}$ of 1.0×10^{-11} cm^3 $molecule^{-1}$ s^{-1} is used in the simulation.

13'. RO_2_C + NO_2 => PAN ($k_{RO_2-NO_2} = 1.0 \times 10^{-11}$ cm^3 $molecule^{-1}$ s^{-1})

The simulation results are presented in Table S9, and the time series of RO_2_C and PAN are shown in Figure S22b. With the inclusion of reaction step 13', we observe the drop of RO_2_C concentrations only by a factor of up to 2 in different aromatic carbonyl oxidation simulations. Figure S22b shows that at 100 ppb NO condition, the average concentrations RO_2_C are 2.60×10^8, 6.83×10^8, and 1.41×10^8 cm^3 $molecule^{-1}$ s^{-1} for BZ, PA, and ACP oxidation, respectively. On the other hand, the average concentrations of PAN (maximum) are 1.02×10^{10}, 2.71×10^{10}, and 5.47×10^9 cm^3 $molecule^{-1}$ s^{-1} for BZ, PA, and ACP oxidation, respectively, at 100 ppb NO condition. Because the primary source of acyl peroxy radical is the aldehydic H abstraction by OH in BZ and PA but not in ACP (see branching ratios in Tables S1–3, Section S3), the actual PAN concentrations formed via reaction step 13' are less than values reported here. This implies that despite the formation of PAN, the concentrations of peroxy radicals produced in the studied systems are significant enough to follow further oxidation and form HOMs as observed experimentally. Note that in the simulation model the influence of NO is reflected as the suppression of peroxy radicals RO_2_C as expected and hence the experimental observation of its enhancing effect on HOM likely involves alkoxy (RO) mediated chemistry that is not included in the model. Incorporating the RO mediated complex chemistry in the model will require extensive molecular level quantum chemical calculations which are unfeasible. It is also important to mention that the

concentrations of oxidant OH and primary RO_2_C radicals reported here are at their upper limits as the loss of the radicals to the reactor wall is not accounted.

Table S9. Average concentrations of OH, RO_2 radicals, and PAN produced in different aromatic carbonyl oxidation experiments derived from chemical simulations including the reaction step RO_2_C + NO_2 → PAN under laboratory conditions.

Expt.	**[NO] ppbv**	**[OH] #/cm^3**	**[RO_2_C] #/cm^3**	**[PAN] #/cm^3**
BZ	50	2.35×10^7	6.19×10^8	1.33×10^{10}
	100	2.00×10^7	2.60×10^8	1.02×10^{10}
	500	8.11×10^6	2.14×10^7	1.83×10^9
	1000	4.99×10^6	6.60×10^6	3.55×10^8
PA	50	1.62×10^7	1.57×10^9	3.38×10^{10}
	100	1.46×10^7	6.83×10^8	2.71×10^{10}
	500	7.98×10^6	7.38×10^7	6.31×10^9
	1000	5.86×10^6	2.74×10^7	1.47×10^9
ACP	50	4.11×10^7	3.56×10^8	7.63×10^9
	100	3.29×10^7	1.41×10^8	5.47×10^9
	500	1.07×10^7	9.19×10^6	7.87×10^8
	1000	5.90×10^6	2.55×10^6	1.36×10^8

Therefore, in our flow reactor experiments, the concentrations of the reactive radical species are very close to the expected concentrations in the ambient air, and we believe they are well representative.

S11.3 From laboratory conditions to urban atmospheric conditions

We observe rapid formation of HOM from aromatic carbonyl OH oxidation reactions in as low as sub-second timescale for PA, conducted in the laboratory flow reactor setup. To inspect the feasibility of HOM formation from OH initiated oxidation of aromatic carbonyls (BZ, PA, and ACP) in the ambient air, we simulate the oxidation reactions under atmospherically relevant conditions of the studied VOCs and reactive partners. The ambient concentrations of these aromatic carbonyls are less than 1 ppb.[18,19] However, in indoor air, the concentrations can be significantly higher emitting from heated electronics, and consumer products. For example, in products like detergents, lotions, and perfumes, the concentrations of acetophenone can range from several tens to hundreds of ppm.[20] In our simulation, considering a polluted urban atmosphere, the initial concentration aromatic carbonyl is given 1ppb (2.46×10^{10} molecules cm^{-3}). A generic concentration of oxidant [OH] = 1.0×10^7 molecules cm^{-3} is used. Two different concentrations of NO (0.1 and 1 ppb, i.e., 2.46×10^9, and 2.46×10^{10} molecules

cm^{-3}) are used to mimic moderately clean to polluted NO_x conditions. Considering a lower limit of atmospheric RO_2 as 1.0×10^7 molecules cm^{-3} in VOC limited condition and a higher limit of atmospheric RO_2 as 1.5×10^9 molecules cm^{-3} in NO_x limited condition, we use a generic value of $[RO_2] = 5.0 \times 10^8$ molecules cm^{-3} in the simulation. We also consider that the carbon centered radical intermediates can readily add an oxygen molecule forming alkyl (or acyl) peroxy radicals (RO_2 or $RC(O)O_2$) via fast pseudo-unimolecular reactions and hence we skip the reaction step for simplification as explained earlier. In a first set of simulations, we run reaction steps 1–6 (see below) and estimate the average concentrations of primary peroxy radicals RO_2_C. Knowing the branching ratios of OH addition to the *ipso* position of different aromatic carbonyls which are 2.64, 4.80, and 18.71 % respectively for BZ, PA, and ACP (see Section S3 above), we consider that roughly 1 % of RO_2_C goes to *ipso* bicyclic peroxy radical (*ipso*-BPR) intermediate in BZ and PA oxidation, and 10 % of RO_2_C goes to *ipso*-BPR in ACP oxidation processes. Accordingly, in a second set of simulations, we give relevant initial concentration of BPR and run the whole reaction scheme (steps 1–10 below) to estimate the production of O_8 HOM from PA and ACP. The *ipso*-BPR molecular rearrangement reaction rates $k_{BPR-MR-C2}$ of 5.0×10^{-3}, 0.6, and 5.3×10^{-3} s^{-1} are used for BZ, PA, and ACP, respectively, obtained from our quantum chemical computations. The subsequent 1,6 H-shift rate coefficient $k_{1,6\,H-shift}$ were computed for PA and ACP to compare the speediness of their overall autoxidation rates. These rates explain the difference in the influence of NO between the two aromatic carbonyls observed experimentally. The HOM_O_8 (reaction step 10 below) is shown to produce directly after the 1,6 H-shift reaction of BPR_C2. Here, a pseudo-unimolecular O_2 addition reaction (converting O_6 to O_8) is embedded in that reaction step. We did not compute the 1,6 H-shift rate coefficient after the BPR rearrangement for BZ. Therefore, in the case of BZ, we run the simulation with reaction steps 1– 9. One example of the reaction steps is as follows:

1. PA + OH => RO_2_C ($k_{PA-OH} = 4.24 \times 10^{-11}$ cm^3 $molecule^{-1}$ s^{-1})
2. NO + OH => HONO ($k_{NO-OH} = 3.3 \times 10^{-11}$ cm^3 $molecule^{-1}$ s^{-1})
3. HONO + OH => H_2O + NO_2 ($k_{HONO-OH} = 6.0 \times 10^{-12}$ cm^3 $molecule^{-1}$ s^{-1})
4. NO_2 + OH => HNO_3 ($k_{NO_2-OH} = 4.1 \times 10^{-11}$ cm^3 $molecule^{-1}$ s^{-1})
5. RO_2_C + RO_2 => Sink_a ($k_{RO_2-RO_2} = 3.2 \times 10^{-11}$ cm^3 $molecule^{-1}$ s^{-1})
6. RO_2_C + NO => $RONO_2$ ($k_{RO_2-NO} = 9.0 \times 10^{-12}$ cm^3 $molecule^{-1}$ s^{-1})
7. BPR => BPR_C2 ($k_{BPR-MR-C2} = 0.6$ s^{-1})
8. BPR + RO_2 => Sink_b ($k_{RO_2-RO_2} = 3.2 \times 10^{-11}$ cm^3 $molecule^{-1}$ s^{-1})

9. BPR + NO => BPR_NO (k_{RO_2-NO} = 9.0 × 10^{-12} cm^3 $molecule^{-1}$ s^{-1})

10. BPR_C2 => HOM_O_8 ($k_{1,6\ H-shift}$ = 0.6 s^{-1})

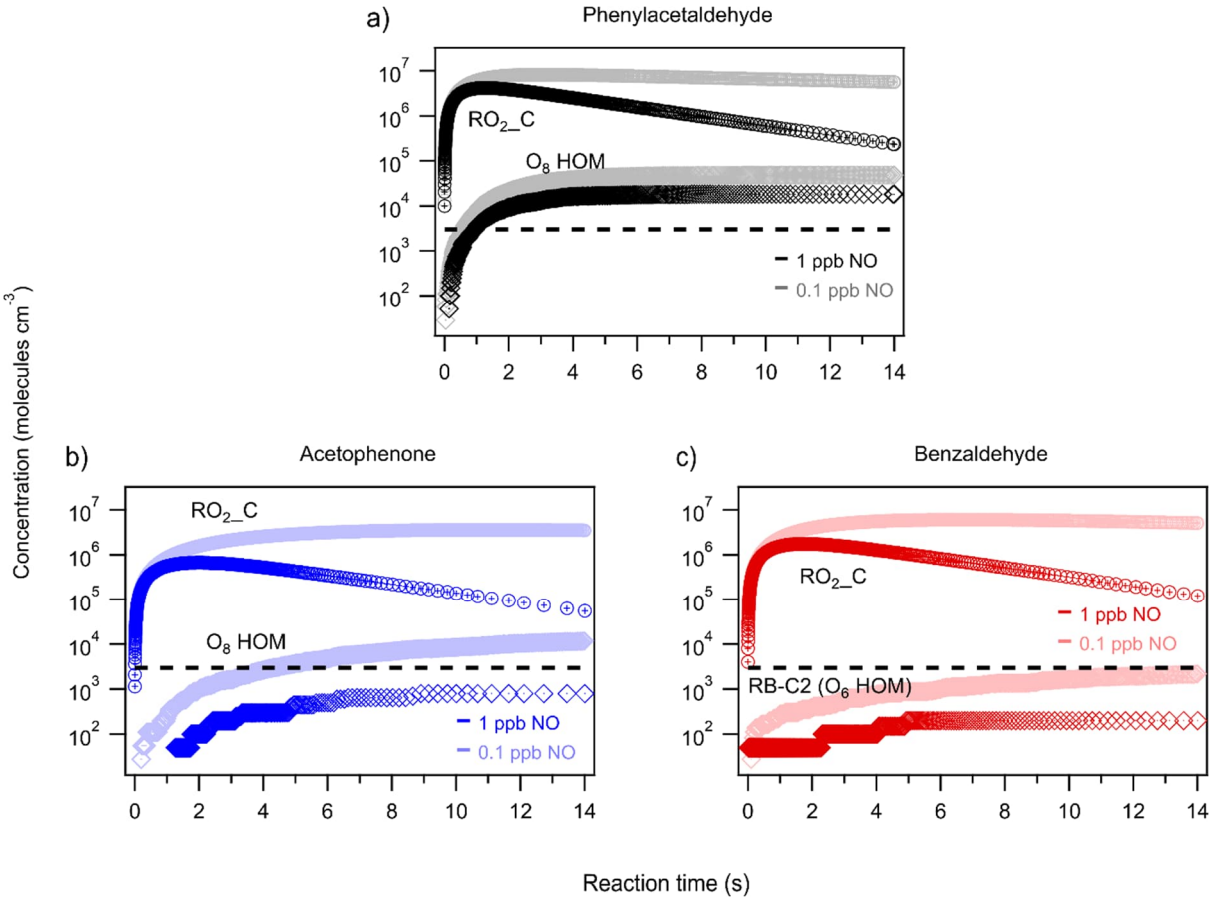

Figure S23. Time series of primary peroxy radicals (RO_2_C) and HOMs produced in aromatic carbonyl OH oxidation reaction simulated under atmospheric conditions (a–c). Reactant concentrations: aromatic carbonyl = 1ppb (2.46 × 10^{10} molecules cm^{-3}), OH = 1.0 × 10^7 molecules cm^{-3}, NO = 0.1, 1 ppb (2.46 × 10^9, 2.46 × 10^{10} molecules cm^{-3}), and RO_2 = 5.0 × 10^8 molecules cm^{-3}. The black dashed line indicating a reference concentration of 3.0 × 10^3 molecules cm^{-3} intersects the product curves at different reaction times. In panel (a), the O_8 HOM reaches the reference concentration before 1 s. In panels (b) and (c), the O_8 HOM and RB-C2 (O_6 HOM), respectively, reach the reference concentration in varying reaction times.

In the case of PA, Figure S23a shows that in reference to a concentration of 3.0 × 10^3 molecules cm^{-3}, O_8 HOM appears in sub-second reaction time in both 0.1 and 1 ppb NO conditions. This observation is completely in line with the experimental observation of HOMs within 0.9 s from PA oxidation initiated by OH. For acetophenone in Figure S23b, the O_8 HOM with a concentration of 3.0 × 10^3 molecules cm^{-3} is formed around 3 s reaction time at 0.1

ppb NO condition, still in close agreement with the experimental observation of HOMs within 2.7s. On the other hand, the production of ring-opened O_6 HOM in BZ oxidation (Figure S23c) seems to be rather slow compared to the experimental observation of HOMs. This is important to note that HOM concentrations in Figure S23 are the lower limits of individual HOM production based on the contribution of only *ipso*-BPR. If there is a possibility of forming HOM from other BPR channels, the actual concentration of these products will be more than what is seen here. In the case of OH initiated oxidation of BZ, the simulation results (concentration of RO_2_C vs O_6 HOM) also indicate that the reaction channel involving the aldehydic H abstraction by OH may contribute to especially C_{x-1} HOM and hence any yet undiscovered pathway along this channel can be of importance. The experimental results shown in Figure 1 (short reaction time experiments) of the main manuscript were conducted without NO addition. However, these simulations that include the reactions of NO with other radical species have only the suppression effect as discussed before. Therefore, it is important to remember the reaction conditions while making a direct comparison between the experiment and simulation. Nevertheless, the fast formation of HOMs in aromatic carbonyl oxidation with OH in the laboratory flow reactor system is very well reflected in the simulation model operated under atmospheric conditions.

References

(1) Jenkin, M. E.; Valorso, R.; Aumont, B.; Rickard, A. R.; Wallington, T. J. Estimation of Rate Coefficients and Branching Ratios for Gas-Phase Reactions of OH with Aliphatic Organic Compounds for Use in Automated Mechanism Construction. *Atmospheric Chem. Phys.* **2018**, *18* (13), 9297–9328. https://doi.org/10.5194/acp-18-9297-2018.

(2) Ziemann, P. J.; Atkinson, R. Kinetics, Products, and Mechanisms of Secondary Organic Aerosol Formation. *Chem. Soc. Rev.* **2012**, *41* (19), 6582. https://doi.org/10.1039/c2cs35122f.

(3) Iyer, S.; Kumar, A.; Savolainen, A.; Barua, S.; Daub, C.; Pichelstorfer, L.; Roldin, P.; Garmash, O.; Seal, P.; Kurtén, T.; Rissanen, M. Molecular Rearrangement of Bicyclic Peroxy Radicals Is a Key Route to Aerosol from Aromatics. *Nat. Commun.* **2023**, *14* (1), 4984. https://doi.org/10.1038/s41467-023-40675-2.

(4) Calvert, J. G.; Mellouki, A.; Orlando, J. J.; Pilling, M. J.; Wallington, T. J. *The Mechanisms of Atmospheric Oxidation of the Oxygenates*; Oxford scholarship online; Oxford University Press: New York, 2020. https://doi.org/10.1093/oso/9780199767076.001.0001.

(5) Nannoolal, Y.; Rarey, J.; Ramjugernath, D. Estimation of Pure Component Properties. *Fluid Phase Equilibria* **2008**, *269* (1–2), 117–133. https://doi.org/10.1016/j.fluid.2008.04.020.

(6) Compernolle, S.; Ceulemans, K.; Müller, J.-F. EVAPORATION: A New Vapour Pressure Estimation Methodfor Organic Molecules Including Non-Additivity and Intramolecular Interactions. *Atmospheric Chem. Phys.* **2011**, *11* (18), 9431–9450. https://doi.org/10.5194/acp-11-9431-2011.

(7) Myrdal, P. B.; Yalkowsky, S. H. Estimating Pure Component Vapor Pressures of Complex Organic Molecules. *Ind. Eng. Chem. Res.* **1997**, *36* (6), 2494–2499. https://doi.org/10.1021/ie950242l.
(8) Pankow, J. F.; Asher, W. E. SIMPOL.1: A Simple Group Contribution Method for Predicting Vapor Pressures and Enthalpies of Vaporization of Multifunctional Organic Compounds. *Atmospheric Chem. Phys.* **2008**, *8* (10), 2773–2796. https://doi.org/10.5194/acp-8-2773-2008.
(9) Stolzenburg, D.; Wang, M.; Schervish, M.; Donahue, N. M. Tutorial: Dynamic Organic Growth Modeling with a Volatility Basis Set. *J. Aerosol Sci.* **2022**, *166*, 106063. https://doi.org/10.1016/j.jaerosci.2022.106063.
(10) Mohr, C.; Thornton, J. A.; Heitto, A.; Lopez-Hilfiker, F. D.; Lutz, A.; Riipinen, I.; Hong, J.; Donahue, N. M.; Hallquist, M.; Petäjä, T.; Kulmala, M.; Yli-Juuti, T. Molecular Identification of Organic Vapors Driving Atmospheric Nanoparticle Growth. *Nat. Commun.* **2019**, *10* (1), 4442. https://doi.org/10.1038/s41467-019-12473-2.
(11) Bunker, D. L.; Garrett, B.; Kleindienst, T.; Long, G. S. Discrete Simulation Methods in Combustion Kinetics. *Combust. Flame* **1974**, *23* (3), 373–379. https://doi.org/10.1016/0010-2180(74)90120-5.
(12) Gillespie, D. T. A General Method for Numerically Simulating the Stochastic Time Evolution of Coupled Chemical Reactions. *J. Comput. Phys.* **1976**, *22* (4), 403–434. https://doi.org/10.1016/0021-9991(76)90041-3.
(13) Atkinson, R.; Arey, J. Atmospheric Degradation of Volatile Organic Compounds. *Chem. Rev.* **2003**, *103* (12), 4605–4638. https://doi.org/10.1021/cr0206420.
(14) Manion, J. A.; Huie, R. E.; Levin, R. D.; Burgess Jr, D. R.; Orkin, V. L.; Tsang, W.; McGivern, W. S.; Hudgens, J. W.; Knyazev, V. D.; Atkinson, D. B.; Chai, E.; Tereza, A. M.; Lin, C.-Y.; Allison, T. C.; Mallard, W. G.; Westley, F.; Herron, J. T.; Hampson, R. F.; Frizzell, D. H. NIST Chemical Kinetics Database, NIST Standard Reference Database 17, Version 7.0 (Web Version), Release 1.6.8, Data Version 2015.09, National Institute of Standards and Technology, MD. **2015**.
(15) Atkinson, R.; Baulch, D. L.; Cox, R. A.; Crowley, J. N.; Hampson, R. F.; Hynes, R. G.; Jenkin, M. E.; Rossi, M. J.; Troe, J. Evaluated Kinetic and Photochemical Data for Atmospheric Chemistry: Volume I - Gas Phase Reactions of O_x, HO_x, NO_x and SO_x Species. *Atmospheric Chem. Phys.* **2004**, *4* (6), 1461–1738. https://doi.org/10.5194/acp-4-1461-2004.
(16) Berndt, T.; Scholz, W.; Mentler, B.; Fischer, L.; Herrmann, H.; Kulmala, M.; Hansel, A. Accretion Product Formation from Self- and Cross-Reactions of RO_2 Radicals in the Atmosphere. *Angew. Chem. Int. Ed.* **2018**, *57* (14), 3820–3824. https://doi.org/10.1002/anie.201710989.
(17) Jenkin, M. E.; Valorso, R.; Aumont, B.; Rickard, A. R. Estimation of Rate Coefficients and Branching Ratios for Reactions of Organic Peroxy Radicals for Use in Automated Mechanism Construction. *Atmospheric Chem. Phys.* **2019**, *19* (11), 7691–7717. https://doi.org/10.5194/acp-19-7691-2019.
(18) Ho, K. F.; Lee, S. C.; Louie, P. K. K.; Zou, S. C. Seasonal Variation of Carbonyl Compound Concentrations in Urban Area of Hong Kong. *Atmos. Environ.* **2002**, *36* (8), 1259–1265. https://doi.org/10.1016/s1352-2310(01)00570-2.
(19) Uebori, M.; Imamura, K. Analysis of Aliphatic and Aromatic Carbonyl Compounds in Ambient Air by LC/MS/MS. *Anal. Sci.* **2004**, *20* (10), 1459–1462. https://doi.org/10.2116/analsci.20.1459.
(20) Yang, B.; Liang, A.; Wang, L. The Atmospheric Oxidation Mechanism of Acetophenone Initiated by the Hydroxyl Radicals. *Atmos. Environ.* **2023**, *309*, 119905. https://doi.org/10.1016/j.atmosenv.2023.119905.

572